

Temperature micro-mapping in oscillatory-zoned chlorite: Application to study of a green-schist facies fault zone in the Pyrenean Axial Zone (Spain)

VINCENT TRINCAL^{1,*}, PIERRE LANARI², MARTINE BUATIER¹, BRICE LACROIX³,
DELPHINE CHARPENTIER¹, PIERRE LABAUME⁴ AND MANUEL MUÑOZ⁵

¹UMR Chrono-Environnement, Université de Franche-Comté, 16 Route de Gray, 25030 Besançon, France

²Institute of Geological Sciences, University of Bern, Baltzstrasse 1+3, CH-3012 Bern, Switzerland

³Department of Earth and Environmental Sciences, University of Michigan, Ann Arbor, Michigan 48109, U.S.A.

⁴Géosciences Montpellier, UMR 5243, Université de Montpellier-CNRS, 34095 Montpellier, France

⁵Institut des Sciences de la Terre, CNRS, Université Grenoble 1, 38041 Grenoble, France

ABSTRACT

Oscillatory compositional zoning in minerals has been observed in hydrothermal, magmatic, and metamorphic environments and is commonly attributed to chemical or physical cyclical changes during crystal growth. Chemical zoning is a common feature of solid solutions, which has been rarely reported in phyllosilicates. In this study, oscillatory zoning in chlorite is described in samples from the Pic-de-Port-Vieux thrust, a minor thrust fault associated to the major Gavarnie thrust fault zone (Central Pyrenees, Spain). The Pic-de-Port-Vieux thrust sheet comprises a 1–20 m thick layer of Triassic red pelite and sandstone thrust over mylonitized Cretaceous dolomitic limestone. The thrust fault zone deformation comprises secondary faults and cleavage affecting the Triassic pelite and sandstone. An important feature responsible to this deformation is a set of veins filled by quartz and chlorite. Chlorite is present in crack-seal extension veins and in shear veins; both structures opened under the same stress conditions. In some shear veins, chlorite occurs as pseudo-uniaxial plates arranged in rosette-shaped aggregates. These aggregates appear to have developed as a result of radial growth of the chlorite platelets. Oscillatory zoning has been imaged by backscattered scanning electron microscopy and by X-ray quantitative micro-mapping. These oscillations correspond to chemical zoning with alternating iron-rich and magnesium-rich bands. The chlorite composition ranges from a Fe-rich pole to a Mg-rich pole. $\text{Fe}^{3+}/\Sigma\text{Fe}$ values were measured in chlorite using μ -XANES spot analyses and vary from 0.23 to 0.44. The highest values are in the Fe-rich area. Temperature maps, built from standardized microprobe X-ray images and redox state using the program XMapTools, indicate oscillatory variations from about 310 to 400 ± 50 °C during chlorite crystallization. These temperature variations are correlated with a $\text{Fe}^{3+}/\Sigma\text{Fe}$ variation by $\text{Al}^{3+}\text{Fe}^{2+}$ and ditrioctahedral substitutions highlighted by Mg and Fe_{Tot} contents (Fe-Mg zoning). Chemical variations could be then explained by alternation of cooling times and cyclical pulses of a fluid hotter than the host rock. It is however not excluded that kinetic effects influence the incorporation of Mg or Fe during chlorite crystallization.

Keywords: Oscillatory zoning, chlorite, $X_{\text{Fe}^{3+}}$, geothermometer, μ -XANES, X-ray mapping, XMapTools

INTRODUCTION

In sedimentary basins petrophysical characterization of a fault zone and reconstruction of the pressure-temperature evolution during faulting activity are of major interest for both fundamental research and oil industry. Indeed, faults can serve as drains or barriers for crustal fluid flow, including hydrocarbons. They may also record fluid-rock interactions in syntectonic veins (e.g., Lacroix et al. 2014). The fault cores are often mineralized with, among other, clay-rich zones (e.g., Buatier et al. 2012; Lacroix et al. 2012; Leclère et al. 2012; Cantarero et al. 2014; Trincal et al. 2014). The role of authigenic clay growth in clay-bearing fault zones is increasingly recognized as a key to understand the mechanics of brittle faulting and thrusting processes (e.g., Wintsch et al. 1995).

This provides new insights into the ongoing debate about the frictional strength of brittle faults (e.g., Chester et al. 1993; Bos and Spiers 2001; Holdsworth 2004; Haines and van der Pluijm 2012; Leclère et al. 2014). In rare cases, oscillatory-zoned minerals can be observed. These minerals witness fluid-rock interaction processes such as mineralogical reactions and mass transfer assisted by fluids (e.g., Beaufort et al. 2005). Their study allows a better understanding of processes such as pressure-solution, fluid-rock interaction, and recrystallization occurring during thrust faulting.

With the development of electron imaging techniques, chemical zoning patterns in metamorphic, magmatic, and hydrothermal minerals have been increasingly investigated (e.g., Jamtveit et al. 1993; De Andrade et al. 2006; Friel and Lyman 2006; Vidal et al. 2006; Dziggel et al. 2009; Robyr et al. 2009, 2014; Pearce and Wheeler 2010; Blanco-Quintero et al. 2011; Dare et al. 2011; Lanari et al. 2012, 2013, 2014b; Manzotti and Ballèvre 2013;

* E-mail: vincenttrincal@gmail.com

Martin et al. 2013; Zhai et al. 2014). Depending on the geological environments and the minerals involved, chemical zoning reflects time series of equilibrium conditions experienced by the rock. Several parameters such as pressure (P), temperature (T), oxygen fugacity (f_{O_2}), water activity (a_{H_2O}), redox conditions ($X_{Fe^{3+}}$), and bulk-rock (solid) or fluid chemical compositions can be involved. For example, the study of zoned minerals is critical to reconstruct detailed P - T paths of individual samples. In low-grade metamorphic rocks, the diffusion processes are slow enough to preserve successive stages of growth and continuous P - T conditions may be derived by analyzing preserved local equilibria (Lanari et al. 2013 and references therein). According to Kohn (2003) all minerals could show zoning for a particular element or isotope at a given scale, and it is simply a matter of time or analytical precision increase before that zonation is described. Chemical zoning patterns such as concentric zoning may result from successive stages of crystallization. From a macroscopic point of view, the variations in chemical composition from core to rim of minerals result of the variations in the relative proportions in a solid solution between two or more end-member minerals. The final rim may show a reversal trend due to late consumption or resorption during retrograde reactions (Schumacher et al. 1999; Kohn and Spear 2000) and/or weathering, generating pellicular patterns (Delvigne 1998).

Sector or hourglass zoning (Dowty 1976; Kwak 1981) and oscillatory zoning (see Shore and Fowler 1996 for a review) are more complex patterns. Minerals showing oscillatory zoning patterns exhibit repetitious concentric compositional zones, i.e., quasi-cyclic alternation in the chemical compositions. Oscillatory mineral zoning has been reported from open-system environments (e.g., Jamtveit 1991; Jamtveit and Andersen 1992; Jamtveit et al. 1993; Holten et al. 2000) in magmatic, metamorphic, and hydrothermal rocks. Occurrences have been found in at least 75 rock-forming and accessory minerals comprising most major chemical groups: silicates (hydrous and anhydrous), sulfides, oxides, halides, carbonates, phosphates, and sulfates (Shore and Fowler 1996). The study of magmatic minerals showing oscillatory zoning allows a deeper understanding of magma evolution during the crystallization of the rock (Putirka and Tepley 2008 and references therein). The best candidate is plagioclase because its composition is sensitive to T , P , and H_2O content of the melt (Shcherbakov et al. 2011). Recent studies interpreted the oscillatory-zoning patterns in plagioclase as convection of crystals across distinct zones of the magmatic chamber before eruption (Nicotra and Viccaro 2012), or by frequent replenishments of the magma chamber causing thermal and chemical interactions between melts and the growing crystals (Shcherbakov et al. 2011). Oscillatory zoning patterns in garnet have been extensively studied to track the metamorphic P - T - t path (e.g., Jamtveit and Andersen 1992; García-Casco et al. 2002; Gaidies et al. 2008) or the hydrothermal fluid conditions evolution of skarn deposits (Gaspar et al. 2008). In faults located in low-grade metamorphic environment, minerals showing oscillatory zoning are common (Shore and Fowler 1996). This zoning is due to the effect of large-scale processes (external dynamics) and/or to pattern formation caused by self-organization of the local growth processes (internal dynamic) (Meth and Carlson 2005; Shore and Fowler 1996; Gaspar et al. 2008; Zhai et al. 2014).

The previous studies on minerals showing oscillatory zoning

allow a better understanding of their crystallization mechanisms in magmatic and metamorphic rocks, but are still insufficient to interpret those in phyllosilicates in hydrothermal environments. In most cases, external changes of the fluid compositions are invoked to explain oscillatory zoning patterns (e.g., Holten et al. 1997). In fluid-rich systems, complex zonings are commonly interpreted to reflect changes in fluid composition or varied degrees of fluid buffering (e.g., Yardley et al. 1991; Beaufort et al. 2005; Jourdan et al. 2009). However, recent experimental studies showed that rapid fluid-flow reactions and ultra-local kinetic effects could lead to fluids with locally extreme non-equilibrium compositions (Borg et al. 2014).

Phyllosilicate are highly sensitive to P - T - X conditions making them good candidates to geothermobarometry purposes (Vidal et al. 2001, 2005, 2006; Inoue et al. 2009; Bourdelle et al. 2013; Lanari et al. 2014a). For example, chlorite polytypes may crystallize at different temperature conditions (Hayes 1970; De Caritat et al. 1993; Walker 1993) ranging from 40 °C in diagenetic sandstones (Hillier and Velde 1991) to 600 °C in high-grade metapelites (Vidal et al. 2001). The chemical variations of chlorite are governed by three main substitutions that are not related to pressure variations (e.g., Shata and Hesse 1998; Zane et al. 1998; Vidal et al. 2001; Lanari et al. 2014b), (1) the Tschermak substitution (TS), which consists in the combined substitution of one divalent cation (Fe^{2+} or Mg^{2+}) and one Si^{4+} for two aluminum cations [$Al^{IV}Al^{VI}Si_{-1}(Mg,Fe)_{-1}$], (2) the Fe^{2+} - Mg^{2+} substitution (FM), (3) the di-trioctahedral substitution, which consists in the substitution of three Mg^{2+} and/or Fe^{2+} cations for two Al^{VI} cations leading to the formation of a vacant site [$(Mg^{2+},Fe^{2+})_3\Box_{-1}Al_2$]. In addition, chlorite can incorporate ferric iron in its brucite-like layer by aluminum-iron substitution (De Grave et al. 1987; Vidal et al. 2005, 2006; Muñoz et al. 2006, 2013; Lanari et al. 2014a). A challenging issue is therefore to measure the $X_{Fe^{3+}}$ ($Fe^{3+}/\Sigma Fe$)_{chl} of chlorite to calculate the correct structural formula.

In chlorite minerals, an important and unanswered question is to determine which mechanisms and parameters control the formation of oscillatory zoning. To address this question, we performed detailed X-ray electron probe microanalysis (EPMA) mapping coupled with $X_{Fe^{3+}}$ Fe K-edge X-ray absorption near edge structure (XANES) measurements on zoned chlorite crystals from the Pic-de-Port-Vieux thrust, in the Axial Zone of the Pyrenees (Spain).

GEOLOGICAL BACKGROUND AND DESCRIPTION OF THE SAMPLES

The Pyrenean belt is a double-vergence orogenic wedge formed during the collision of the Iberian and European plates between the Late Cretaceous and the early Miocene (e.g., Muñoz 1992; Roure et al. 1989; Teixell 1998). The south-vergent thrust system comprises imbricated basement thrusts, which form the anticlinal stack of the Axial Zone and pass southward to detachment levels within the sedimentary cover thrust units of the South-Pyrenean Zone (Fig. 1a). The studied area is located in the Pyrenean Axial Zone, in the eastern slope of the Pic-de-Port-Vieux (Fig. 1b). The major structure in this area is the Gavarnie thrust (GT), involving a minimum southward displacement of 11.5 km (Grant 1989) of Upper Paleozoic strata on Hercynian to Lower Paleozoic basement covered with Permo-Triassic and Upper Cretaceous strata (Fig. 1c). The Gavarnie thrust activity is dated from the Priabonian to

Rupelian by stratigraphy in the South-Pyrenean foreland basin (Teixell 1996) and to the Priabonian (36.5 ± 1.4 Ma) by ^{40}Ar - ^{39}Ar isotopic dating on authigenic illite from the thrust fault zone (Rahl et al. 2011). The latter authors also report a Maastrichtian (ca. 70 Ma) age but the Jaca basin stratigraphic organization make it difficult to relate this age to an early thrusting activity (i.e., the future Gavarnie thrust sheet area was tilting northward down to basal depths at that time, e.g., Teixell 1996). In the Pic-de-Port-Vieux culmination, a secondary thrust occurs in the footwall of the Gavarnie thrust: the Pic-de-Port-Vieux (PPV) thrust (Fig. 2). With a minimum southward displacement of 0.85 km (Grant 1990), the PPV thrusting deformed, and is thus younger than, the Gavarnie thrust and emplaced Triassic pelites/sandstones above Upper Cretaceous dolomitic limestone (Figs. 2 and 3a).

Structures and microstructures related to the PPV thrust emplacement have been extensively studied by Grant (1990, 1992). In the hanging-wall of the major thrust surface, a damage zone about 10 m thick comprises four generations of extensional normal faults (Fig. 3c; see Grant 1992 for details). The last generation corresponds to low-angle synthetic normal faults (Fig. 3c) related to the reactivation of the PPV thrust by spreading/gliding inducing shear and extension strain (Grant 1992). During this tectonic episode, previously formed (pre-thrusting and syn-thrusting) high-angle faults were reactivated as conjugated normal faults. The formation of these normal faults records syn-kinematic fluid-rock interactions in chlorite \pm quartz \pm calcite extension veins and shear veins (Fig. 3b, Grant 1992). Forty samples were collected, for most of them, in faults and veins in the hanging-wall of the PPV thrust. The stars in Figure 3c indicate the positions of zoned

chlorite crystals, systematically localized in the largest synthetic faults (labeled A and B in Fig. 3c).

METHODS

Analytical techniques

Detailed investigation of textures, microstructures, and related variations of chemistry in chlorite was conducted using optical microscopy and scanning electron microscope (SEM) coupled with energy-dispersive spectrometer (EDS) analyses. Quantitative chemical analyses were performed by electron probe micro-analysis (EPMA).

SEM observations were performed with a JEOL JSM5600 scanning electron microscope coupled with a FONDIS energy-dispersive analyzer (EDS) at the Renatech network Femto laboratory (University of Franche-Comté). More detailed observations were made with a JEOL JSM 6400F at the Institut Carnot de Bourgogne (University of Bourgogne).

Quantitative chemical analyses of zoned chlorite minerals were performed using two JEOL 8200 EPMA at ISTE (University of Lausanne) and at the Institute of Geological Sciences (University of Bern). X-ray compositional maps were measured using wavelength-dispersive spectrometers (WDS) and analytical conditions of 15 keV accelerating voltage, 100 nA specimen current, 300–450 ms dwell time, and 1 μm spot size. Punctual analyses were acquired at the Institute of Geological Sciences (University of Bern), using common standards: albite (Si), phlogopite (K), ilmenite (Fe, Ti), orthoclase (Ca, Al), spinel (Mg), tephroite (Mn), and enstatite (Cr) with 15 keV accelerating voltage, 10 nA specimen current, and 40 s dwell time.

Chemical analyses of unzoned chlorite crystals were performed using a CAMECA model SX100 electron microprobe equipped with five WDS at the University of Montpellier. The microprobe was operated at 20 keV accelerating voltage, with a specimen current of 10 nA and a beam diameter of 3 μm . The used standards were albite (Na), Al_2O_3 (Al), Fe_2O_3 (Fe), forsterite (Mg), orthoclase (K), TiO_2 (Ti), and wollastonite (Si, Ca) (for the choice of the standards see Merlet and Bodinier 1990).

To determine the speciation of iron in chlorite crystals, Fe K-edge XANES and X-ray fluorescence (XRF) data were collected at the BM23 beamline of the European Synchrotron Radiation Facility (ESRF; Grenoble, France) using the micro-focused experimental setup. The storage ring was operating in the 16-bunch mode with an

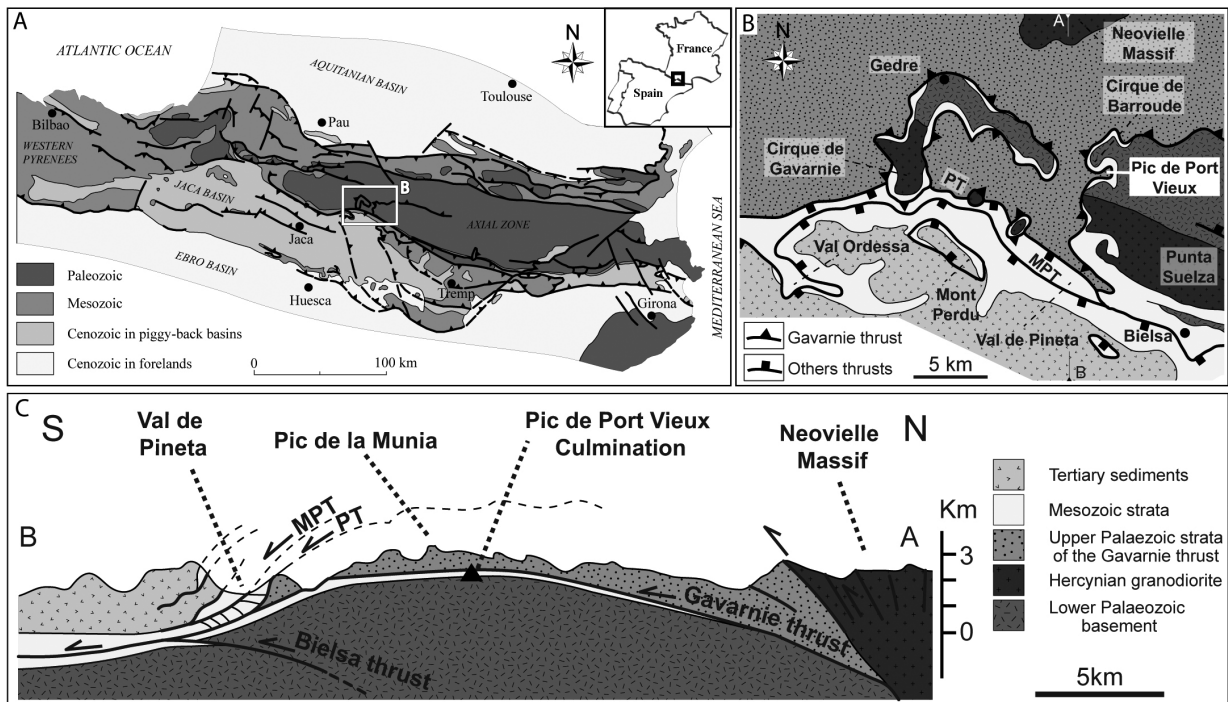


FIGURE 1. (a) Structural map of the Pyrenees with the location of study area (modified from Teixell 2000). Geological map (b) and (c) cross-section AB of the Gavarnie thrust sheet showing the location of the study area (Pic-de-Port Vieux) modified from Grant (1992) and Jolivet et al. (2007). MPT = Monte Perdido thrust; PT = Pineta thrust.

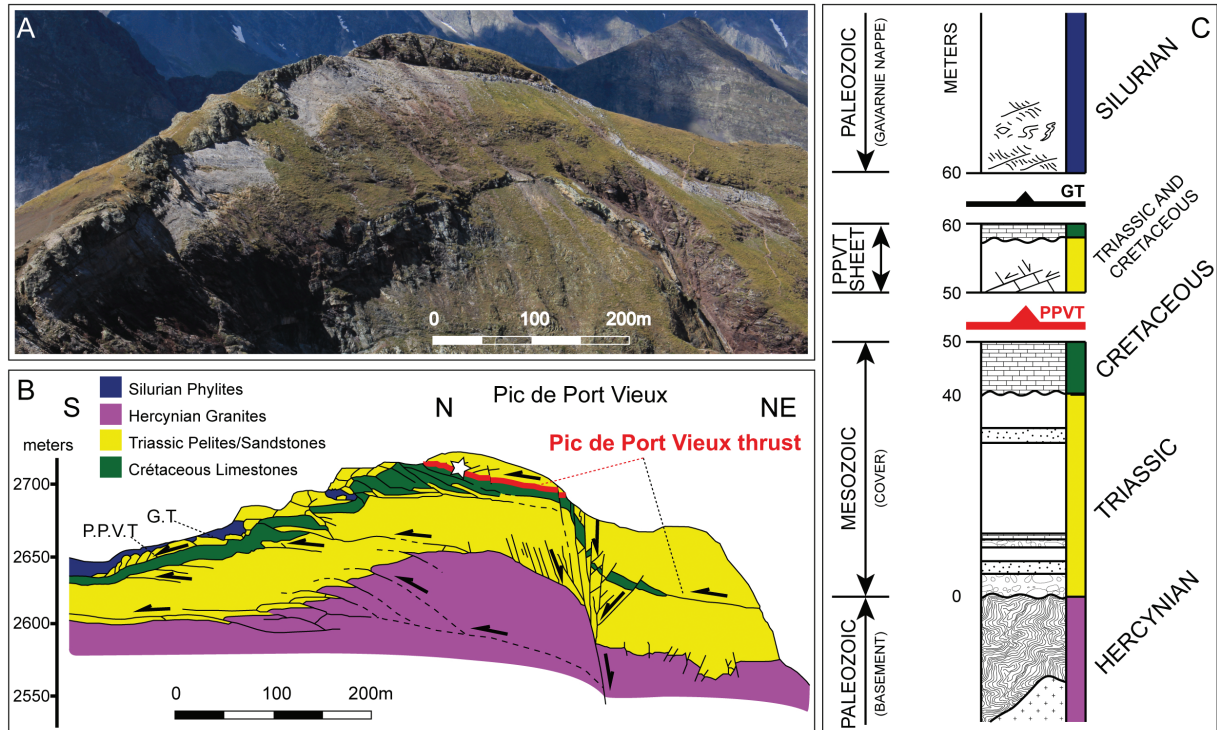


FIGURE 2. (a) View of the Pic-de-Port-Vieux massif. (b) Pic-de-Port-Vieux thrust culmination showing the main study area, modified from Grant (1989). (c) Schematic stratigraphic log through the Pic-de-Port-Vieux culmination, modified from Grant (1990). GT = Gavarnie Thrust; PPVT = Pic-de-Port-Vieux Thrust.

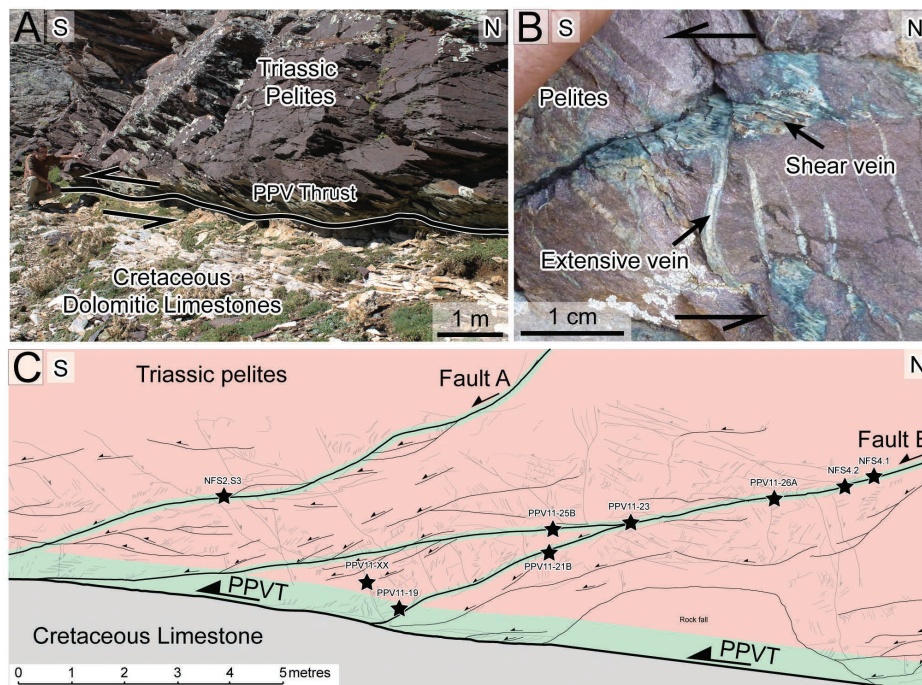


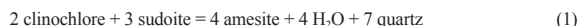
FIGURE 3. (a) Pic-de-Port-Vieux outcrop showing hanging-wall Triassic pelites and footwall Cretaceous dolomitic limestone separated by the PPV thrust. (b) Outcrop view of shear and extension veins filled by quartz and chlorite in hanging wall Triassic pelites. (c) Detailed sketch of synthetic faults (faults A and B); others faults and veins are indicated in gray (color) (modified from Grant 1989). Stars = samples with oscillatory-zoned chlorite, from Grant (1989) (NF) and from this study (PPV). Red and green colors correspond to red pelite and altered green pelite, respectively.

average current of 75 mA. X-rays were generated using a bending magnet, and monochromatized with a double crystal fixed exit Si(111) monochromator. Micro-focusing KB mirrors were used to focus the beam down to $4 \times 4 \mu\text{m}$ full-width half maximum (FWHM). Data were collected in fluorescence mode using a Vortex silicon-drifted diode located at 85° of the incident X-ray beam. The samples were positioned perpendicular to the X-ray beam to minimize self-absorption (Pfalzer et al. 1999). μ -XRF maps were first recorded at 9 keV, with $10 \mu\text{m}$ spatial resolution, and a dwell time of 0.5 s. Then, μ -XANES spectra were collected at the Fe *K*-edge for different locations of the XRF maps. Data normalization and pre-peak fits were performed with the XasMap package, originally dedicated to the dispersive micro-XANES mapping applications (Muñoz et al. 2006, 2008). The Fe *K*-edges were fitted between 7108 and 7118 eV using three pseudo-Voigt functions, following the procedure of Muñoz et al. (2013). To derive the speciation of iron, pre-edge calibration was based on the following powdered standards: staurolite ($^{IV}\text{Fe}^{2+}$), siderite ($^{VI}\text{Fe}^{2+}$), andradite ($^{VI}\text{Fe}^{3+}$), and sanidine ($^{VI}\text{Fe}^{3+}$), according to Wilke et al. (2001). Chlorite crystals were oriented in the magic angle geometry to prevent polarization effects in the XANES and pre-edge regions (i.e., crystal orientation relative to the polarized X-ray beam), in agreement with Muñoz et al. (2013).

Data processing and thermometry calculation

X-ray images data were processed using the program XMapTools 1.6.5 (Lanari et al. 2014b). The allocation of each pixel to one mineral phase (e.g., chlorite or quartz) was done using all the elements analyzed by EPMA. Chlorite X-ray raw intensity of Si, Al, Ti, Fe, Mg, Mn, Ca, Na, Cr, and K were converted into oxide wt% compositions SiO_2 , Al_2O_3 , TiO_2 , FeO , MgO , MnO , CaO , Na_2O , Cr_2O_3 , and K_2O using internal standards, i.e., transects of point analyses measured on the same area (De Andrade et al. 2006). Indeed, the reduction of acquisition time at 200 ms per pixel allows significant time saving in the map creation, but requires standardization with well-localized spot analyses using a standard EPMA setup. The “automatic median” approach available in XMapTools was used (Lanari et al. 2014b). The quality of the standardization was tested by comparing the composition of the internal standard and the composition of the corresponding pixel in the X-ray maps. Chlorite structural formulas were then calculated for each pixel using the function available in XMapTools. This function allows calculating a structural formula on a 14 oxygen-basis by distributing elements on two tetrahedral (T1, T2) and three octahedral sites (M1, M2M3, M4) and assuming equipartition between Fe^{2+} and Mg^{2+} [constant $X_{\text{Mg}} = \text{Mg}^{2+}/(\text{Mg}^{2+} + \text{Fe}^{2+})$ on M1, M2, M3, and M4]. The knowledge of the iron oxidation state [$X_{\text{Fe}^{3+}} = \text{Fe}^{3+}/(\text{Fe}^{3+} + \text{Fe}^{2+})$] of chlorite is required to calculate the correct structural formula of chlorite without the hypothesis of $\Sigma\text{Fe} = \text{Fe}^{2+}$. It has been shown that incorporation of Fe^{3+} instead of Fe^{2+} may generate important changes of the calculated X_{Mg} and the amount of vacancy (\square) in M1 (Vidal et al. 2005; Lacroix et al. 2012; Lanari et al. 2014a). End-member proportions of amesite, clinocllore, daphnite, and sudoite were estimated from the abundance of Al, Mg, Fe^{2+} , and \square in the M1 site, respectively.

Maps of formation temperature can be calculated from the oxide wt% maps using the different empirical and semi-empirical calibrations available in XMapTools (Lanari et al. 2014b). In this study, we used a calibration that allows the chlorite temperature calculation knowing $X_{\text{Fe}^{3+}}$. Among the two recent calibrations using $X_{\text{Fe}^{3+}}$ adapted to low-grade metamorphism context (Inoue et al. 2009 and Lanari et al. 2014a), we used the calibration Chl(1) from Lanari et al. (2014a) that was better constrained, in particular with an adjustment of the standard state thermodynamic properties of sudoite. The calibration of Inoue et al. (2009) gives similar results. The Lanari et al. (2014a) calibration is based on the following chlorite + quartz + water equilibrium:



Ideal activities of amesite, clinocllore, and sudoite are calculated using a site mixing model for chlorite end-members and $a_{\text{H}_2\text{O}} = 1$ (Lanari et al. 2014a), which allows the determination of $\ln(K)$ using the following equation:

$$\ln(K) = \ln(a_{\text{ame}}^4/a_{\text{chl}}^2 a_{\text{sud}}^3). \quad (2)$$

Chlorite temperatures are then calculated using:

$$T_{\text{chl}} (\text{°C}) = 17234 / [-\ln(K) + 315.149] - 273.15 \quad (3)$$

An average temperature was calculated from quadrat samples of $20 \times 20 \mu\text{m}$ (corresponding to 400 pixels) using a Monte Carlo technique (1000 permutations for each pixel corresponding to 400000 calculations) to simulate the uncertainty of 5% on the $X_{\text{Fe}^{3+}}$ determined by μ -XANES measurements. The center of the quadrat location was superimposed to the XANES-related point. According to the number

of data and the small heterogeneities of the sample, a 1σ standard deviation appears significant and was calculated for each quadrat.

RESULTS

Host rock

The Pic-de-Port-Vieux thrust fault zone comprises pelites in the hanging-wall and dolomitic limestone in the footwall (Fig. 4a). Pelite is constituted by phyllosilicates (mainly illite-muscovite, but also chlorite), quartz, and dispersed grains of hematite, apatite, and rutile (Fig. 4b); rare calcite is detected. Near the major thrust surface and along synthetic faults, the red pelite turns to a greenish color. The green pelite is characterized by the absence of hematite (Fig. 4c). Illite-muscovite is still abundant. Matrix quartz displays an elongated morphology with long axis parallel to schistosity. Chlorite crystallized commonly along extension veinlets and shear veinlets (Fig. 4c). In the footwall, the dolomitic limestone is composed of euhedral dolomite crystals in a microcrystalline calcite matrix with rare iron oxides (Fig. 4d). Approaching the thrust surface, dolomitic limestone is progressively mylonitized (Fig. 4a). Dolomite is progressively dissolved (Figs. 4e and 4g) and secondary calcite precipitated in dolomitic ghosts and cracks (Fig. 4f). Within the mylonite, dolomite occurs only as anhedral remains in calcite.

Chlorite description

Two types of chlorite minerals crystallized in the Pic-de-Port-Vieux veins related to synthetic fault activity. Figures 5a and 5b shows a syntaxial extension vein filled by quartz + chlorite \pm calcite. In these veins, chlorite crystals are preferentially developed along the vein-host rock interface and quartz crystals occur as elongated crystal with axis perpendicular to the vein boundaries. These textural observations suggest that chlorite nucleated first in contact to the host-pelite and grew toward the center of the vein with a growth direction parallel to the schistosity planes. When a vein crosses pelite and silt alternating layers, chlorite is preferentially present along the pelitic layers (Figs. 5a and 5b). In these extension veins, quartz shows parallel inclusion bands (dust or secondary minerals inclusions parallel to the vein wall) and serrated grain boundaries (called “radiator structure” within Bons et al. 2012) indicating a crack-seal mechanisms of vein formation (Ramsay 1980). The second type of vein corresponds to shear vein filled by quartz, chlorite, and locally calcite (Figs. 5c and 5d). The quartz exhibits blocky crystals without any preferential orientation. Moreover, chlorite occurs sometime in these shear veins as pseudo-uniaxial plates arranged in rosette-shaped aggregates. These structures suggest that chlorite is followed by quartz during precipitation of these minerals in open fractures. These two vein types are cogenetic and in accordance with the orientation of the principal axes of the local field stress (Fig. 5e).

SEM images show that rosette chlorite from shear veins displays oscillatory zoning pattern (Fig. 6a) while chlorite from extension veins is homogenous. The rosette-like morphology of chlorite can be seen on Figures 6b and 6c. Both images show that the rosettes correspond to the aggregation of individual platelet crystals composed of stacks of layers 20–50 μm thick and 100–200 μm long. This morphology suggests that chlorite grew in an open space and that quartz crystallization postdates chlorite growth as discussed above. However, the contacts between quartz and chlorite grains are devoid of any corrosion texture (Figs. 6a and 6c).

Within a single vein, all chlorite aggregates exhibit similar zon-

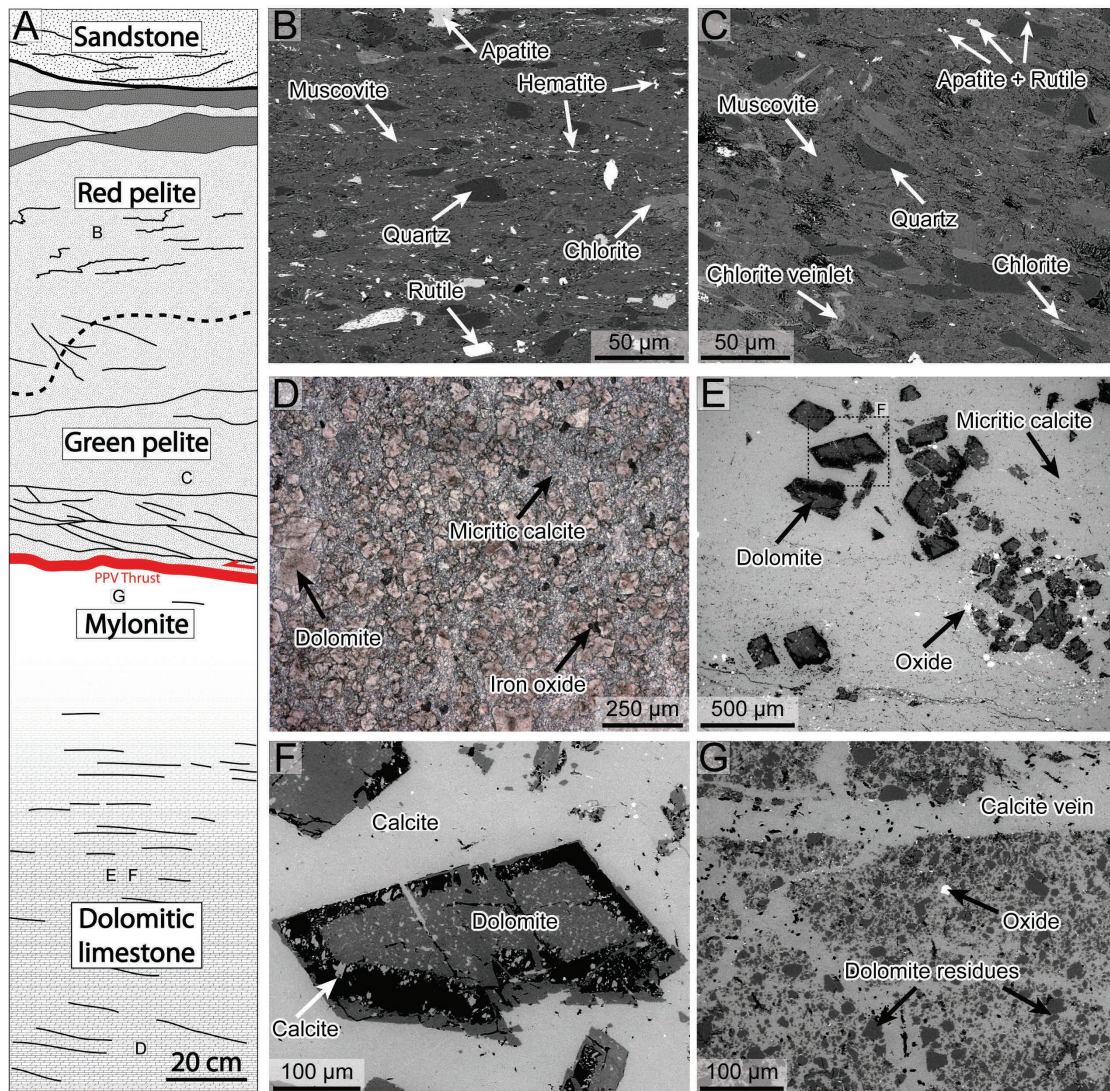


FIGURE 4. (a) Schematic diagram of the structural organization of the studied fault zone outcrop. (b) SEM image of pelite showing quartz, muscovite, chlorite, hematite, rutile, and apatite minerals; PPV12-06B sample. (c) SEM image of green pelite with almost the same mineralogy as B except for missing hematite; PPV12-05 sample. (d) Optical microscopic image from dolomitic limestone showing euhedral dolomite in micritic calcite matrix; PPV11-01 sample. (e) SEM image of euhedral dolomite and iron oxides in micritic calcite. (f) Zoom from e on a dolomite crystal partially dissolved in calcite matrix. Newly formed calcite precipitated inside dolomitic cracks and dissolution ghosts (in black). (g) SEM image of a fractured and microveined dolomitic limestone sampled close to thrust in the footwall.

ing patterns with the same number of contrasted layers. However, the thickness of the layers can vary from one rosette to another (Fig. 6a). At higher magnifications, the zonation appears complex with heterogeneous contrasts at the micrometric scale (Fig. 6d). The contrast distribution appears as stair steps in section, seeming to follow the growth development of the chlorite crystals (layer by layer or by spiral growth) but with preferential growth directions perpendicular to c^* [F face is (001)] (Fig. 6e).

Chlorite chemistry

Two X-ray images were performed on aggregates of oscillatory-zoned chlorite from a shear vein using EPMA (maps A and B, Fig. 7). Five zones are distinguishable in the two aggregates. Zone 1

is located in the core of the aggregate and zone 5 in the external rim (Figs. 7b). Backscattering oscillatory contrasts are caused by FeO and MgO content variation (Figs. 7c and 7d). FeO and MgO contents display strong opposite behaviors with absolute variations up to 7 wt%. FeO ranges from 16 to 23 wt% and MgO from 21 to 13 wt%. SiO₂ and Al₂O₃ contents show smaller variations (less than 2 wt%). SiO₂ ranges from 25 to 27 wt% and Al₂O₃ from 22 to 24 wt% (Figs. 7e and 7f). There is a slight increase of Al₂O₃ from zone 1 (core) to zone 4, whereas the external rim (zone 5), like zone 1, displays lower Al₂O₃. SiO₂ content is almost constant in all zones, except in zone 2 where it is about 2 wt% higher. X-ray image from chlorite extension veins was not performed due to the chemical homogeneity of these minerals.

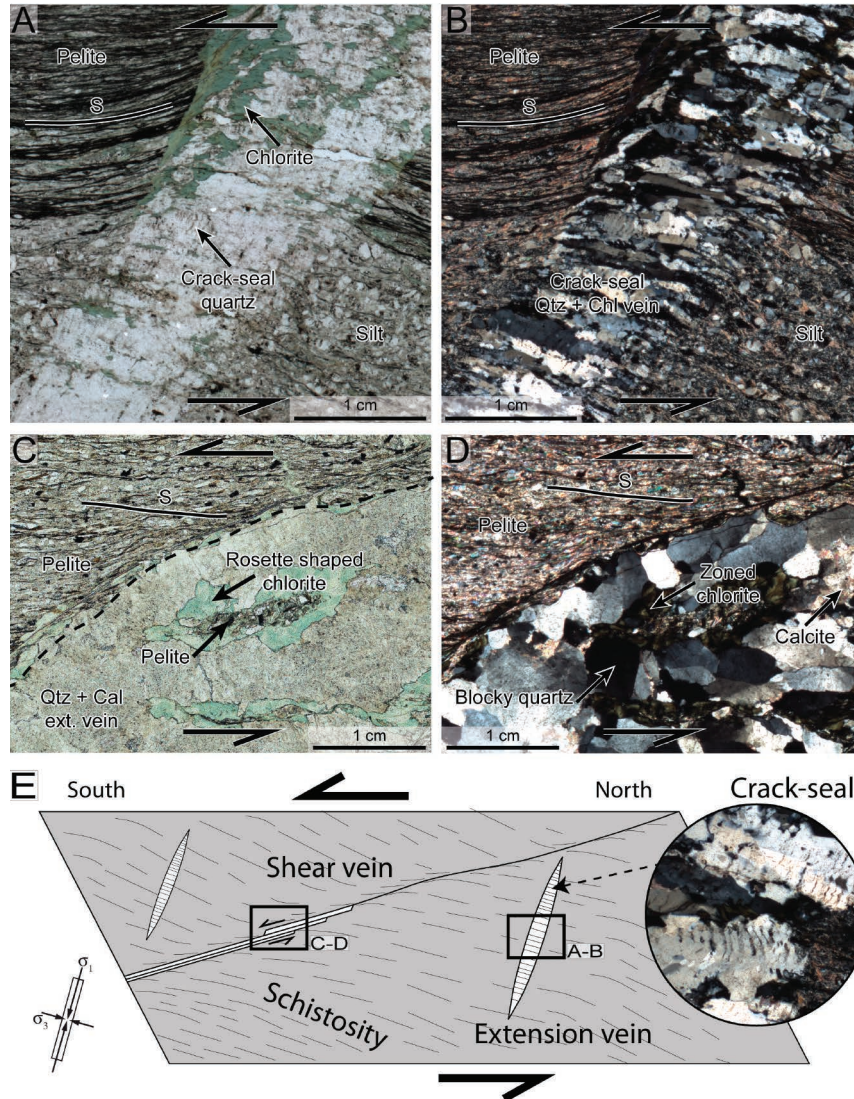


FIGURE 5. Microscopic observation of thin sections from the studied fault zone: (a–b) quartz + chlorite ± calcite extension crack-seal syntaxial vein showing chlorite nucleation in contact with host-pelite preferentially to silt; in PPL and XPL, respectively from sample PPV11-11B; (c–d) shear vein showing blocky quartz ± calcite crystal textures and rosette-shaped zoned chlorite; in PPL and XPL, respectively, from sample PPV11-25B. (e) Representative sketch of veins cogenetic to synthetic fault. In extension veins, quartz crack-seal appears parallel to the vein wall. Key: S = schistosity plane; PPL = plane-polarized light; XPL = cross polarized light.

Based on both μ -XRF and EPMA chemical maps, μ -XANES measurements were performed in five spots along a radius of zoned chlorite mineral that was previously analyzed (Fig. 8a). Normalized spectra are displayed in Figure 8b. Spectral signatures are typical of clinocllore (e.g., Muñoz et al. 2013). Their similar shape suggests that similar crystal orientations are considered for these measurements. However the Xan1 spectrum shows a slightly different shape suggesting a small change in orientation, mostly because it is located in the center of the concentric crystal. According to the work of Muñoz et al. (2013), this shape might lead to a slight overestimation of the $X_{\text{Fe}^{3+}}$ (i.e., $\text{Fe}^{3+}/\Sigma\text{Fe}$) from the pre-edge data reduction. But according to the same authors, this overestimation should not exceed 0.07, which is in the same

range of the typical accuracy of the method (± 0.05).

Figure 8c shows the baseline-subtracted pre-edge peaks (white circles), together with their best fits (solid lines) and pseudo-Voigt peaks used for deconvolution (dotted lines). Results in terms of integrated area and centroid energy positions are displayed in the variogram of Figure 8d. The accuracy of the centroid value is ± 0.05 eV (Muñoz et al. 2013). This variogram also shows reference values obtained for the standard compounds (white circles) used for the calibration of the data (see Wilke et al. 2001 for details). Results obtained for the different locations along the radius of the crystal all plot in between the two octahedral Fe^{2+} – Fe^{3+} end-members, in agreement with the structure of clinocllore crystals (i.e., Fe located in octahedral sites). The conversion into $X_{\text{Fe}^{3+}}$ show

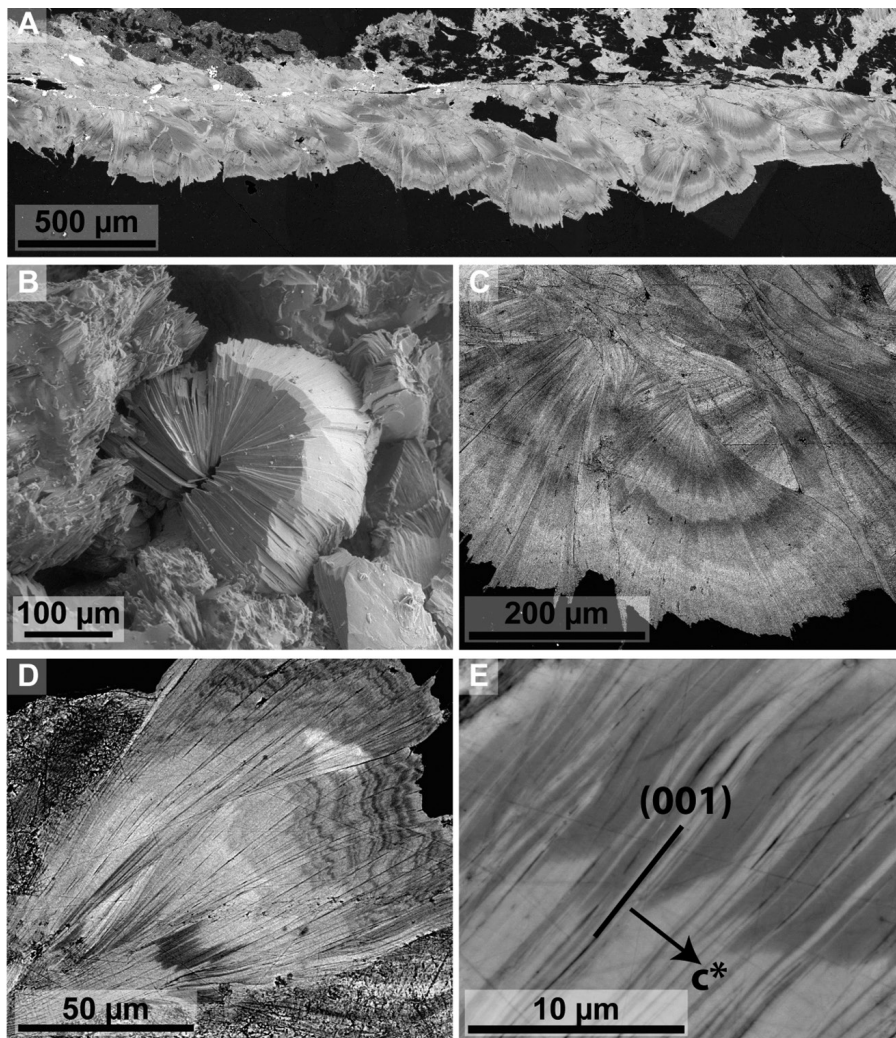
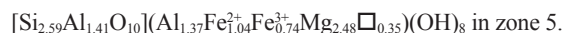
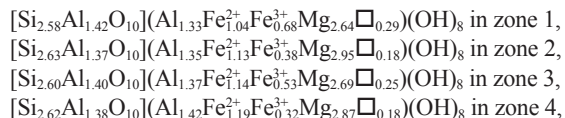


FIGURE 6. (a) SEM images of oscillatory zoning pattern chlorite crystals from sample PPV11-XX. The rosette like morphology of the chlorite aggregates is imaged (b) in 3D on PPV11-16 sample and (c) in thin section on sample PPV11-19. (d) Contrasted layers can have different thickness from one rosette to another and zonation can be complex as imaged in sample PPV11-25B. (e) At a higher magnification, the contrast distribution seems to follow the growth development of the chlorite crystals but with preferential growth directions as highlighted in sample PPV11-25B.

periodic variations ranging from 23 to 44% ($\pm 5\%$). In addition to the integrated area and the centroid position values, Table 1 shows the $X_{\text{Fe}^{3+}}$ values obtained from XANES normalization.

Assuming that each zone has homogeneous iron state oxidation, μ -XANES measurements (Table 1) coupling with quantitative oxide wt% composition maps (Fig. 7) were used to calculate structural formulas for each pixel of chlorite (from a shear vein) using “Chl-StructForm.m” function of XMapTools (Lanari et al. 2014b). $X_{\text{Fe}^{3+}}$ values from chlorite Map A are assumed to be the same as for Map B. In each zone from chlorite Maps A and B, representative structural formulas were given in Table 2 and plotted in Figure 9. The average composition in Map A are:



Two groups can be distinguished from these results. The first group includes structural formulas from zones 1, 3, and 5; they correspond to Fe-rich chlorite (Fig. 9a). Their compositions are closed to the unzoned chlorite (homogenous, without chemical variation) from synkinematic extension veins and correspond to 40% of clinocllore+daphnite, 40% of amesite, and 20% of sudoite (Fig. 9b). The second group is enriched in Mg and corresponds to the analyses of the zones 2 and 4 (Fig. 9a). Their compositions are out of the field of unzoned chlorite and correspond to 20–30% of clinocllore+daphnite, 40% of amesite, and 30–40% of sudoite (Fig. 9b). The differences between the two chlorite groups are the Mg- Σ Fe substitution in octahedron (Fig. 9a) and also a ditrioctahedral substitution (Fig. 9b). No Tschermak substitution has to be invoked to explain the chemical variations.

Chlorite structural formulas are calculated from each pixel of

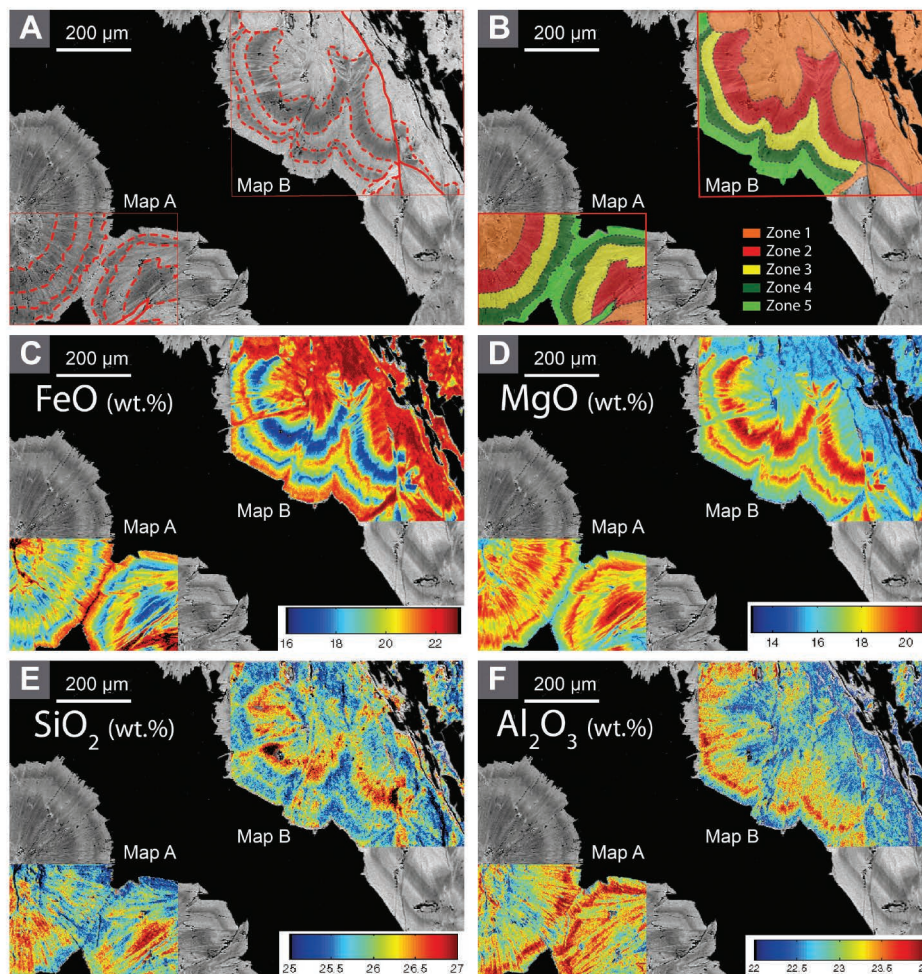


FIGURE 7. Microprobe X-ray (WDS) images from sample PPV11-XX. Values of each box are reported Table 1. (a) SEM-BSE image of the analyzed area. (b) Zones 1 to 5 defined from a based on electronic contrast. (c) FeO in wt%. (d) MgO in wt%. (e) SiO₂ in wt%. (f) Al₂O₃ in wt%.

the analyzed area, allow building of Fe²⁺, Fe³⁺ maps (Figs. 10a and 10b). In zones 1 and 5, Fe²⁺ content is equal to 1 apfu while it reaches 1.1 to 1.2 in zones 2, 3, and 4. Fe³⁺ is equal to 0.8 apfu in zones 1 and 5; 0.7 apfu in zone 3 and 0.6 apfu in zones 2 and 4. Fe²⁺ content shows small variations probably due to edge effect (the X_{Fe³⁺} between two successive zones probably gradually changing), it may be considered constant throughout the crystallization. In contrast, Fe³⁺ content displays strong variations. These results highlight an iron redox change during crystal growth, with a cyclic alternation between more ferrous and more ferric chlorite layers.

To test whether the FM substitution is at the origin of the zonation between Fe-rich and Mg-rich layers, an X_{Mg} = Mg²⁺/(Mg²⁺+Fe²⁺) map has been produced (Fig. 10c). In agreement with structural formulas (Table 2), X_{Mg} map (Fig. 10c) does show significant variation. X_{Mg} is constant around 0.72 ± 0.03.

Temperature map

Temperature map (Fig. 10d) is derived using the Equation 3, which is the thermometer Chl(1) from Lanari et al. (2014a) in XMapTools using the X_{Fe³⁺} measurements for each zone (Table 1). In both Maps A and B, average temperatures with associated

uncertainty were estimated and are reported in Table 2. For both aggregates, temperatures were estimated at 307 ± 19 to 347 ± 27 °C in zone 1, followed by 370 ± 36 to 396 ± 29 °C in zone 2, 338 ± 24 to 354 ± 23 °C in zone 3, 402 ± 49 to 405 ± 41 °C in zone 4, and 316 ± 20 to 320 ± 22 °C in zone 5. Chlorite crystals A and B display the same temperature evolution: they show a series of warming and cooling cycles during crystallization. The temperature oscillation (up to 100 °C range) is correlated to the chemical zonation: Mg-rich layers correspond to hot areas while Fe-rich layers correspond to cold ones.

DISCUSSION

Chlorite chemical zoning described above is characterized by Fe-Mg chemical variations and increase in Fe³⁺ in the Fe-rich layers. These chemical changes may reflect changes of local equilibrium conditions experienced during PPV thrust activity. Several parameters such as pressure (*P*), temperature (*T*), oxygen fugacity (*f*_{O₂}), water activity (*a*_{H₂O}), redox conditions (X_{Fe³⁺}), and bulk system composition (including bulk-rock and fluid compositions) could be invoked to explain the zoning. In the section below, we discuss the effect of those parameters on the chlorite compositions

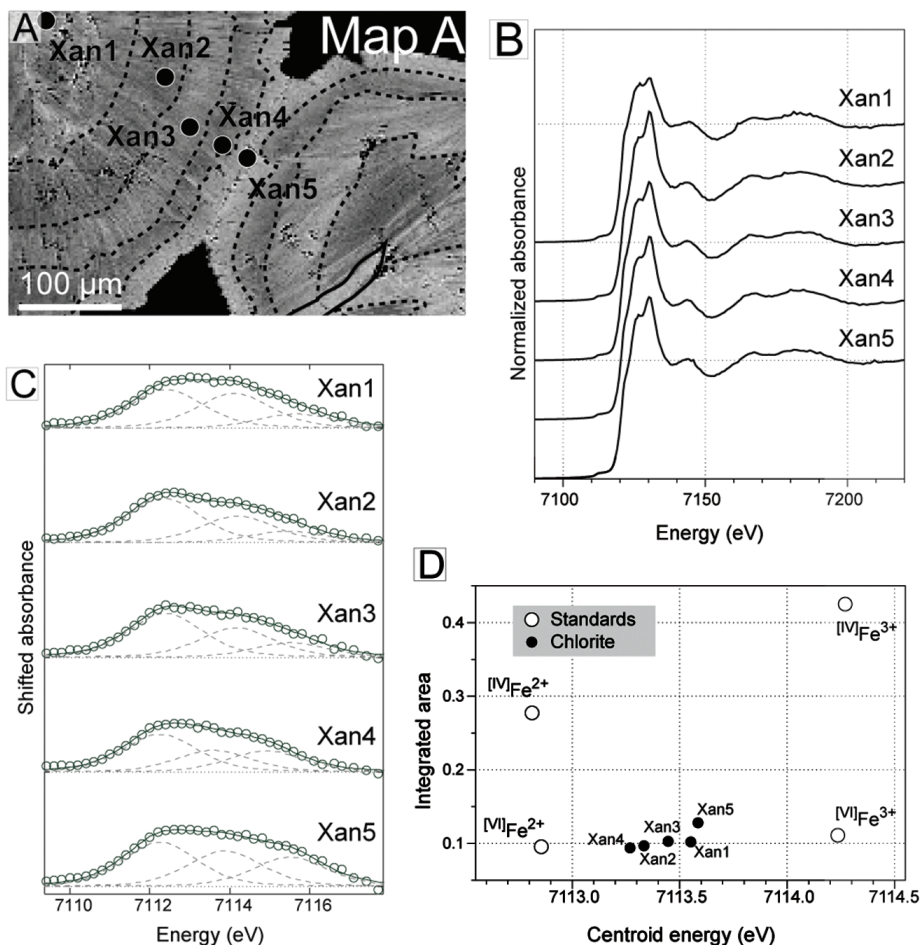


FIGURE 8. (a) Scheme of the mapped area showing growth bands in clinoclone concentric crystal (sample PPV11-XX Map A), and the locations of μ -XANES measurements; (b) corresponding normalized XANES spectra; (c) baseline-subtracted pre-edge peaks (white circles), best fits (solid lines), and peaks used for deconvolution (dashed lines); (d) integrated area vs. centroid position variogram showing the positions of standards together with the data from clinoclone crystal. Values are reported Table 1 and converted in $X_{\text{Fe}^{3+}}$ based on the calibration curve of Wilke et al. (2001).

TABLE 1. Results from XANES and pre-edge spot analyses, showing the integrated area and centroid position of pre-edge peaks and $X_{\text{Fe}^{3+}}$ values obtained from XANES normalization

Spot	Integrated area	Centroid energy (eV)	$X_{\text{Fe}^{3+}}$
Xan1	0.1021	7113.55 ± 0.05	42(7)
Xan2	0.0969	7113.33 ± 0.05	27(5)
Xan3	0.1029	7113.45 ± 0.05	34(5)
Xan4	0.0940	7113.27 ± 0.05	23(5)
Xan5	0.1281	7113.59 ± 0.05	44(5)

to discriminate, which can have played a critical role during the growth of these aggregates.

Significance of chemical and temperature oscillations registered by PPV thrust chlorite aggregates

Chlorite chemistry can be a very good indicator of temperature of crystallization (e.g., Cathelineau and Nieva 1985; Cathelineau 1988; De Caritat et al. 1993; Vidal et al. 2001, 2005, 2006; Inoue et al. 2009; Bourdelle et al. 2013; Lanari et al. 2014a). In this study, the calibration Chl(1) of Lanari et al. (2014a) is used to calculate the formation temperature of chlorite for a known $X_{\text{Fe}^{3+}}$ content

(obtained by μ -XANES). Temperature oscillations between ~ 310 and ~ 400 °C are found in correlation to chemical variations for the two studied chlorite aggregates. The core of the chlorite aggregates (zone 1) and the last rim (zone 5) with low-Mg and high- Fe^{3+} chemical composition recorded the lowest temperatures (~ 310 °C). These two zones correspond to the first and last stages of crystallization, respectively. Between these two zones (i.e., zones 2, 3, and 4) the crystallization temperature oscillates between 350–400 °C with the highest temperatures corresponding to the layers with the highest Mg and lowest Fe^{3+} contents, respectively.

The 1σ standard deviation on the average temperature of each growing zone is reported in Table 2 and Figure 11. Such large errors could indicate that all the zones crystallized around 350 ± 50 °C if this standard deviation is considered to be representative of the analytical uncertainty. However, temperature differences are significant between the different zones as supported by the temperature map in Figure 10d. The large 1σ deviations calculated in this study are caused by the ultra-local chemical variability occurring within each zone. As the standard deviation on the temperature is calculated from a local area (see methods), grain boundaries

TABLE 2. Chlorite structural formulas from sample PPV11-XX Maps A and B

Zones	Map A					Map B					Unzoned
	1A	2A	3A	4A	5A	1B	2B	3B	4B	5B	
SiO ₂	25.17(49)	26.11(36)	25.74(33)	25.98(43)	25.53(44)	25.76(33)	26.39(37)	25.75(34)	25.85(39)	25.55(33)	26.57(71)
TiO ₂	0.01(0)	0.01(0)	0.01(0)	0.01(0)	0.01(0)	0.02(0)	0.01(0)	0.02(0)	0.01(1)	0.02(0)	0.03(8)
Al ₂ O ₃	22.76(52)	22.93(29)	23.25(32)	23.65(56)	23.16(46)	22.91(42)	23.00(41)	23.17(39)	23.55(43)	23.05(41)	22.91(66)
FeO	20.98(88)	18.43(76)	20.43(62)	18.39(91)	21.94(81)	21.92(42)	17.59(48)	20.47(45)	18.70(77)	21.48(42)	24.27(176)
MgO	17.27(76)	19.64(63)	17.86(54)	19.09(75)	16.41(65)	16.36(43)	19.83(54)	17.44(45)	18.83(70)	16.58(42)	14.54(136)
MnO	0.09(3)	0.09(3)	0.09(3)	0.09(3)	0.08(3)	0.10(2)	0.11(2)	0.11(2)	0.11(2)	0.11(2)	0.05(5)
CaO	0.02(1)	0.01(0)	0.01(0)	0.01(0)	0.01(0)	0.01(0)	0.01(0)	0.01(0)	0.01(0)	0.01(0)	0.03(4)
Na ₂ O	0.02(0)	0.02(0)	0.02(0)	0.02(0)	0.02(0)	0.03(1)	0.03(1)	0.03(1)	0.03(1)	0.03(1)	0.00(2)
Cr ₂ O ₃	0.05(2)	0.05(2)	0.05(2)	0.05(2)	0.04(2)	0.05(1)	0.05(1)	0.05(1)	0.05(1)	0.05(1)	
K ₂ O	0.01(0)	0.01(0)	0.01(0)	0.01(0)	0.01(0)	0.01(0)	0.01(0)	0.01(0)	0.01(0)	0.01(0)	0.03(14)
Σ	86.37(116)	87.29(54)	87.47(53)	87.30(131)	87.23(96)	87.17(76)	87.02(74)	87.04(73)	87.15(72)	86.87(70)	88.20(112)
Si	2.58(3)	2.63(2)	2.60(3)	2.62(3)	2.59(3)	2.62(3)	2.65(3)	2.62(3)	2.61(3)	2.60(3)	
Al ^{IV}	1.42(3)	1.37(2)	1.40(3)	1.38(4)	1.41(3)	1.38(3)	1.35(3)	1.38(3)	1.39(3)	1.40(3)	
Al ^{VI}	1.33(4)	1.35(3)	1.37(3)	1.42(5)	1.37(4)	1.37(3)	1.38(4)	1.39(3)	1.42(4)	1.37(3)	
Fe ²⁺	1.04(5)	1.13(5)	1.14(4)	1.19(6)	1.04(4)	1.08(2)	1.08(3)	1.15(3)	1.22(5)	1.02(2)	
Fe ³⁺	0.68(3)	0.38(2)	0.53(2)	0.32(2)	0.74(3)	0.70(1)	0.36(1)	0.53(1)	0.33(1)	0.72(2)	
Mg	2.64(10)	2.95(8)	2.69(8)	2.87(10)	2.48(10)	2.48(6)	2.97(7)	2.64(6)	2.84(9)	2.52(6)	
Fe ³⁺ /Fe _{tot}	0.42	0.27	0.34	0.23	0.44	0.42	0.27	0.34	0.23	0.44	
Al M1 = X _{Ame}	0.43(3)	0.38(2)	0.40(3)	0.39(3)	0.41(3)	0.39(3)	0.35(3)	0.39(3)	0.39(3)	0.40(3)	
Mg M1 = X _{Clin}	0.20(2)	0.32(2)	0.24(2)	0.31(2)	0.17(2)	0.19(1)	0.33(2)	0.24(2)	0.30(2)	0.18(1)	
Fe M1 = X _{Dph}	0.08(1)	0.12(0)	0.10(0)	0.13(1)	0.07(1)	0.08(1)	0.12(1)	0.10(1)	0.13(1)	0.07(1)	
□ = X _{Sud}	0.29(3)	0.18(2)	0.25(2)	0.18(3)	0.35(3)	0.34(2)	0.19(3)	0.27(2)	0.18(3)	0.34(2)	
X _{Mg}	0.72(2)	0.72(1)	0.70(1)	0.71(2)	0.70(2)	0.70(1)	0.73(1)	0.70(1)	0.70(2)	0.71(1)	
T (°C)	341(26)	396(29)	351(22)	405(56)	312(21)	302(18)	370(36)	336(24)	406(41)	310(19)	

Notes: Unzoned chlorite medians and standard deviation oxides wt% were added for comparison. $X_{Mg} = Mg^{2+}/(Fe^{2+}+Mg^{2+})$. Oxides in wt%, atoms in apfu. Each data represents the average and standard deviation of 400 calculated with Monte-Carlo simulation points corresponding to $20 \times 20 \mu m^2$ in the map. $X_{Fe^{3+}}$ standard deviation induce small variations in the structural formulas; they have not been reported in this table calculated with Monte-Carlo simulation. Points are reported on Figures 9 and 11.

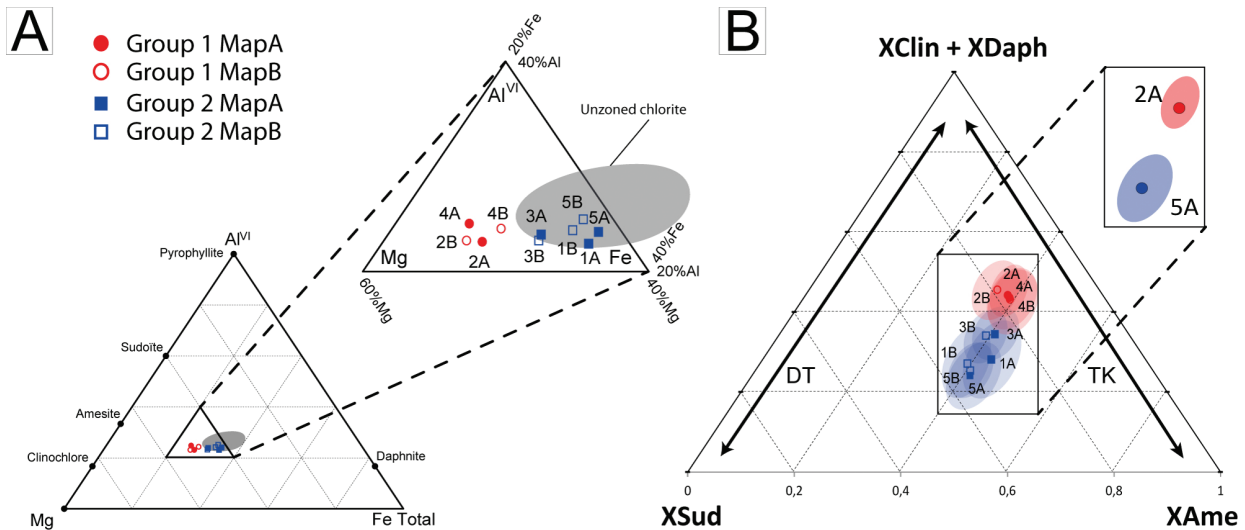


FIGURE 9. Plot of the chlorite compositions from boxes samples in (a) chemical elements of the octahedron; (b) amesite-(clinocllore+daphnite)-sudosite end-member ternary diagram including iron state oxidation data. TK = Tschermak substitution; DT = Ditrioctahedral substitution.

or heterogeneities may cause a large dispersion of values. The temperature map in Figure 10d supports that at the scale of each growth zone, the temperature variation is smaller than around ± 25 °C. Thus, temperature differences highlighted in this study between the different growth zones 1–5, 3, and 2–4 are significant. Although the average temperatures give values from 310 ± 50 to 400 ± 50 °C, it is more accurate to consider a difference of at least 50 °C between the two populations because of the absolute uncertainty of thermodynamic models and mineral compositions.

The lowest temperatures (310 ± 50 °C) recorded during the first and the fifth stages of chlorite growth are similar to those

calculated for unzoned chlorite located in extension and shear veins from the same area (Fig. 9a). These temperatures are consistent with temperature estimation of 250–300 °C based on fluid inclusion microthermometry on quartz from extension vein in the PPV thrust (Grant et al. 1990; Banks et al. 1991; McCaig et al. 2000). They are also consistent with stable isotopic data on quartz and chlorite from the same area, which indicate a temperature of 320 ± 30 °C (Lacroix and Vennemann 2015) and with carbonate footwall temperature obtained with Raman spectroscopy of carbonaceous material (work in progress). In contrast, chlorite layers with higher Mg content are probably formed at higher temperature:

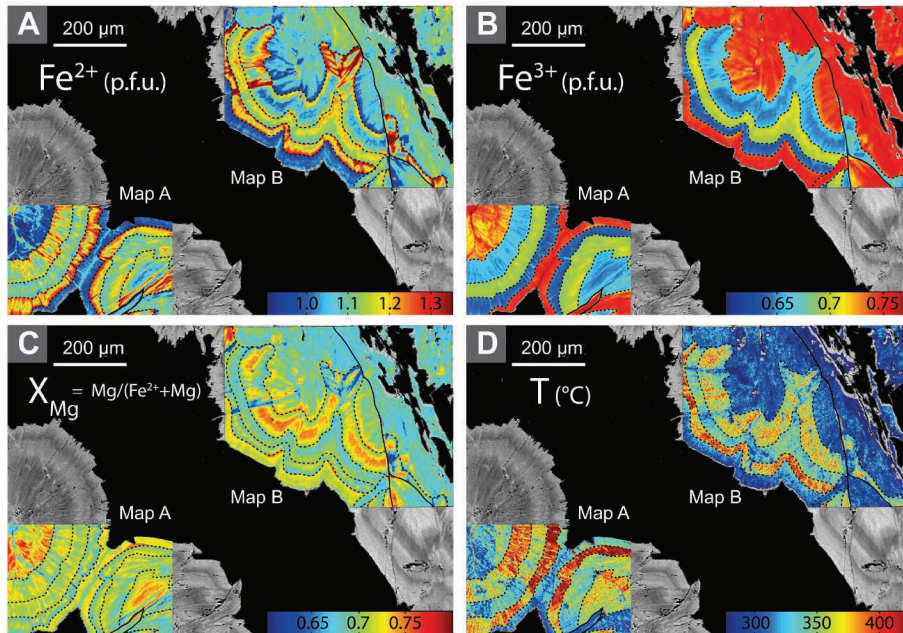


FIGURE 10. Microprobe X-ray images from sample PPV11-XX with $\text{Fe}^{3+}/\text{Fe}_{\text{tot}}$ specific for each chlorite band. Representative values of each zone are reported Table 1. (a) Fe^{2+} in apfu. (b) Fe^{3+} in apfu. (c) $X_{\text{Mg}} = \text{Mg}/(\text{Fe}^{2+}+\text{Mg})$ ratio. (d) Temperature map from Lanari et al. (2014a) model calculation.

400 ± 50 °C. The thermometry results suggest that the minimum ΔT between two successive layers is about 20–30 °C while the likely ΔT in all the chlorite is about 50–80 °C. Such temperature variation is discussed in detail in the following section.

External and internal factors for chemical zonation

Recent studies based on experimental fluid mineral reactions demonstrate that zoning of mineral compositions does not always reflect the evolution of fluid composition (Borg et al. 2014). These authors showed that during rapid fluid-rock reactions, ultra-local fluid composition variation can form complex mineral zoning patterns, even when the overall system is highly fluid-buffered. Wang and Merino (1992) proposed a dynamic model, autonomously able to produce oscillatory zoning of trace elements in calcite without changes in bulk water chemistry. In this model, the growth-induced H^+ buildup at the growth surface of calcite making the surface more positive, thus repelling inhibited cations (such as Mn^{2+}) and accelerating the growth rate. The increase in growth rate in turn further accelerates H^+ accumulation (positive feedback) until the Ca^{2+} concentration becomes depressed next to the surface and slows down the crystallization. Then, H^+ diffusion in fluid makes the surface less positive (or even negative) and allows restarting calcite crystallization with incorporation of inhibiting cations. Another growth cycle is triggered. Previous studies in the PPV thrust reveal a circulation of oilfield brines, highly concentrated in ions (Banks et al. 1991). As the growth of chlorite aggregate is probably very rapid, ultra-local fluid disequilibrium cannot be excluded to explain a part of the observed zonation. However, the chemical oscillation display similar patterns at the vein scale suggesting large crystallization volumes (e.g., Fig. 6a). The scale of zoning is very large and shows significant chemical contrasts. This suggests that oscillatory zoning patterns are not due to local kinetic effects in the PPV thrust faults but to an external parameter such as the variation of the oxygen fugacity.

Beaufort et al. (2005) described zoned chlorite spherules of hydrothermal origin in sandstones near the uranium deposits of the East Alligator Rivers field in Australia. They interpreted the

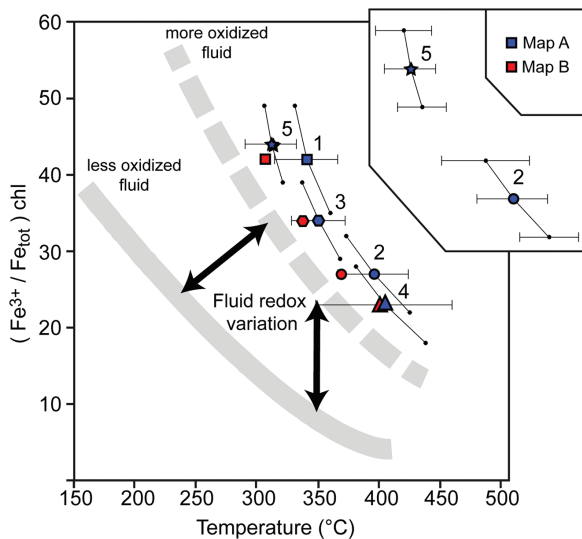


FIGURE 11. Relationships between the $(\text{Fe}^{3+}/\Sigma\text{Fe})_{\text{chl}}$ value in chlorite and the temperatures estimate from the Lanari et al. (2014a) geothermometer. Two main trends were reported from Lanari et al. (2014a) corresponding on two redox conditions of fluid, which are less oxidized (continuous line) and more oxidized (dashed line). Each sample number refers to its zone in Map A (in blue) or in Map B (in red); for example the blue star corresponds to the zone 5 in Map A.

chemical oscillatory zoning in Fe and Mg as the result of periodic changes in physico-chemical condition of the hydrothermal solution during the crystallization process. These authors have performed microprobe measurements to know the chlorite chemistry; they showed significant variations in Mg but were not able to estimate the $X_{\text{Fe}^{3+}}$, which would have allowed a comparison with our data. In the present study, microprobe mapping of chlorite chemistry (atom per formula unit, Fig. 10b) shows significant variations in Fe^{3+} (from 0.6 to 0.75 apfu) during the crystallization. Highest $\text{Fe}^{3+}/\Sigma\text{Fe}$ values correspond to lowest temperatures of chlorite formation. Several authors (Vidal et al. 2006; Tarantola et al. 2009; Grosch et al. 2012; Lanari et al. 2012; Cantarero et al. 2014) found similar correlation between $(\text{Fe}^{3+}/\Sigma\text{Fe})_{\text{chl}}$ and temperature. In all these studies $(\text{Fe}^{3+}/\Sigma\text{Fe})_{\text{chl}}$ was indirectly estimated using the Vidal et al. (2005, 2006) approach. In a review paper, Lanari et al. (2014a) found similar trend using both measured $(\text{Fe}^{3+}/\Sigma\text{Fe})_{\text{chl}}$ and estimated $(\text{Fe}^{3+}/\Sigma\text{Fe})_{\text{chl}}$ using the approach of Vidal et al. (2005, 2006). In a $\text{Fe}^{3+}/\Sigma\text{Fe}$ vs. temperatures diagram (Fig. 11), Lanari et al. (2014a) identified two main trends using chlorite data reported in the literature and calculation from Vidal et al. (2005, 2006). Both trends correspond to chlorite formed under different redox condition, i.e., various samples where chlorite crystallized under less oxidized or more oxidized conditions (see continuous and dashed curves in Fig. 11, respectively). According to these authors, for a given f_{O_2} , chlorite formation temperature may control the amount of Fe^{3+} input in the structure. In other words, the amount of Fe^{3+} in chlorite cannot be considered alone without a formation temperature as a proxy for the redox conditions. Estimated T and measured $\text{Fe}^{3+}/\Sigma\text{Fe}$ from chlorite of PPV thrust have been reported in this diagram, they are located just above the more oxidized trend (Fig. 11). This result implies that the $\text{Fe}^{3+}/\Sigma\text{Fe}$ variations of chlorite during its crystallization are mainly caused by temperature variations. The redox conditions (f_{O_2}) are the same during the chlorite crystallization history. Indeed, if the f_{O_2} in the fluid would have change during chlorite growth, the point analyses would be more scattered on both redox trends (e.g., arrows in Fig. 11).

ORIGIN OF OSCILLATORY-ZONED CHLORITE AGGREGATES IN THE PPV THRUST VEINS

Previous data and model

Chemistry, source, behavior, and P - T conditions of fluids have been previously investigated from fluid inclusions performed in PPV thrust quartz veins (Grant et al. 1990; Banks et al. 1991; McCaig et al. 1995). Synthetized in McCaig et al. (2000), these analyses reveal at least two distinct fluids. Both of them are hypersaline brines (Banks et al. 1991) with a high Br/Cl ratio indicating seawater evaporation with halite precipitation origin (Banks and Yardley 1992). These brines could have been derived from the upper Triassic evaporites and stored in the lower Triassic redbeds (McCaig et al. 2000). Part of this formation water could have been stored in another rock, such as the Devonian phyllites or the Silurian graphitic slates, inducing a change in the isotopic signature of the fluid (Banks et al. 1991). However, the latter interaction has not been certified because no sample carried from local rocks has sufficiently elevated ratio of all the Pb isotopes to explain the fluid inclusions data (McCaig et al. 2000). According to (Grant 1989), chemical zonation in chlorite could be due to a

mixing of two distinct fluids. Reducing fluid interactions with Triassic pelites would permit the release of Fe^{3+} by hematite dissolution along the PPV thrust and synthetic faults (Fig. 3c) (Beaufort et al. 1992, 2005). Furthermore, the fluid interaction with limestone allows the release of Mg by dolomite dissolution (e.g., Figs. 4f and 4g).

Fluid inclusion microthermometry indicates temperatures never exceeding 300 °C during quartz vein formation (Grant et al. 1990; Banks et al. 1991) and fluid pressure comprised between 1.5 and 2 kbar (Grant 1990), corresponding to a burial depth of 5–7.5 km. Furthermore, measured homogenization temperatures (T_m) define two fluid populations that have been interpreted as a variation of the pressure of 600 bar due to fault valve mechanism (Grant et al. 1990; Banks et al. 1991; McCaig et al. 2000). Indeed, fault-valve process may cause abrupt fluid pressure fluctuations during the thrust activity (Sibson 1990) and have been highlighted by crack-seal structures, open-space filling textures of the quartz + chlorite ± calcite veins and distribution of inclusions in quartz.

New data and model

According to the present study, oscillatory-zoned chlorite from the PPV thrust records cyclic changes in temperature without any change of the fluid redox condition or kinetic disequilibrium. The composition map reported in Figure 10c indicates that $X_{\text{Mg}} [\text{Mg}^{2+}/(\text{Fe}^{2+}+\text{Mg}^{2+})]$ in chlorite does not vary significantly within analytical uncertainties ($X_{\text{Mg}} = 0.70 \pm 0.3$) during the aggregate growth. These results suggest that the X_{Mg} of the system does not change during the crystallization of chlorite (Lanari et al. 2014a and references therein), i.e., the chemical composition of the mineralizing fluid remains constant. Indeed, chlorite is very sensitive to bulk composition changes and its X_{Mg} would be modified in case of alternation of two fluids chemistries during crystallization.

Thus, each vein containing oscillatory chlorite recorded distinct fluid flow history implying a variation of the number and intensity of pulses, but also a variation in the kinetics of cooling and crystallization. On the other hand, fluid inclusions from PPV thrust quartz veins reveal temperatures from 250 to 300 °C, never higher than 325 °C (Grant et al. 1990; Banks et al. 1991; McCaig et al. 2000). Several hypotheses can be raised on these differences. (1) Quartz and zoned chlorite may not be strictly cogenetic. Indeed, in shear veins where zoned chlorites formed, chlorite rosettes are always located against the walls of the veins while quartz is in the center of the veins and fills the open spaces between the chlorite rosettes, suggesting that quartz precipitation postdated chlorite formation. In these conditions, quartz fluid inclusions do not represent the chlorite formation conditions. (2) The two fluid populations recorded by the fluid inclusion study could be related to temperature variation instead of pressure variation, as evocated in Grant et al. (1990). (3) Fluid inclusion and chlorite sampling was not performed in similar veins. Chlorite sampled in crack-seal extension veins and small shear veins gives similar to those obtained by fluid inclusions. In a crack-seal vein, the opening of the crack (before the seal) is very small (of the order of 50 μm or less), the opening mechanism is relatively slow and thus it is impossible to keep a thermal imbalance at this scale. Therefore, crack-seals would likely form during interseismic periods (buildup of stress in the

seismic valve model). In contrast the large shear veins that are characterized by blocky texture would form during more dynamic rupture likely being the break seismic (as suggested by Boullier and Robert 1992). Thus, crack-seal veins open progressively and slowly (opening speed almost equal to the speed of healing, if we integrate all the small increments “cracks” and “seal”). By contrast, large shear veins can be opened by large jolts as suggested by the blocky quartz texture (Figs. 5c and 5d) allowing chlorite crystallization in thermal disequilibrium with host rock.

How to get hot fluid inputs?

The results discussed above suggest that oscillatory-zoned chlorite recorded the temperature variation of one fluid, sometime hot (more than 350 °C) probably episodic and minor; sometime colder reflecting a cooling down to lithostatic equilibrium around 300 °C. The question is how to explain this fast input of hotter fluid? No igneous activity has been reported in this area at this time, so the uniqueness way to introduce a much hotter fluid into the vein would be to move fluid up from deeper fault portions. For a geothermal gradient close to 30 °C/km as estimated in the Jaca basin (Lacroix et al. 2011), at least 2 km of vertical movement, representing 4 km of fluid transport along the Gavarnie thrust considering a dip about 30°, must be invoked. Such fluid transport scale implicates that the fluid had to ascend through a narrow channel way (1) with no loss of heat in contact to the surrounding rocks, implicating quasi-instantaneous emplacement [a 1 cm thick vein will lose most of its excess heat by conduction in few minutes (e.g., Carslaw et al. 1959)]; (2) with channel way heating and in this case the whole chlorite rosette and surrounding rocks for at least several meters will have experienced the peak temperatures estimated. Several investigations can be explored to try to resolve this paradox. It is possible that the geothermal gradient changed at greater depth, reducing the fluid migration distance. Fault-valve process increases the fracture permeability for fluid draining and related shear vein formation. Such process permits a high-temperature fluid discharge in open veins followed by a cooling event in contact to host rock (pelite). This mechanism has been observed by several authors. For example Cantarero et al. (2014) describe high geothermal gradients (50 °C/km minimum) along fractures. Temperature measurements in a fault after an earthquake indicate a slight positive anomaly that can be interpreted by viscous heating (e.g., Brodsky et al. 2009). Strain heating results from the conversion of mechanical energy into heat during progressive deformation and, for some models indicate that temperature rises of a few hundred degrees can be expected in major thrust sheets (Brun and Cobbold 1980; Souche et al. 2013). There is not strain heating evidence in the Pic-de-Port-Vieux thrust, so the ΔT (>20–30 °C) recorded by the chlorite rosettes is most likely related to an increase in the permeability of the fault rock for hot fluids flowing from deeper areas. Fluid flows associated to earthquakes reveal variations of flow rate and fluid sources (e.g., Toutain et al. 1997, 2006; Manga and Wang 2007). For example, Mogi et al. (1989) show hot spring temperature variations related to earthquakes occurrences. These temperature variations can be explained by a model of earthquake-enhanced permeability due to the dislodging of obstacles from clogged fluid channels, such as pre-existing fractures. Unclogged fractures act to breach hydrologic barriers (such as aquitards) and connect

otherwise isolated aquifers or other fluid sources, causing fluid source switching and/or mixing (Wang and Manga 2010). It is thus possible that the ΔT measured in zoned chlorite from the PPV thrust reflects the discharge of a deeper and hotter aquifer by stronger fluid flow during large earthquakes.

IMPLICATIONS

(1) This study shows how important is the measure of $X_{\text{Fe}^{3+}}$ in low-grade metamorphism chlorite to study their chemistry, because the proportion of Fe^{3+} can locally reach up to 45% of the total amount of iron. To measure $\text{Fe}^{3+}/\Sigma\text{Fe}$ ratio XANES and Mössbauer techniques may be used, but microanalyses can only be performed using μ -XANES spectroscopy.

(2) With the development of chlorite thermometry, several models have recently emerged including $X_{\text{Fe}^{3+}}$ estimation (e.g., Vidal et al. 2005, 2006) or requiring the knowledge of the $X_{\text{Fe}^{3+}}$ (Inoue et al. 2009; Lanari et al. 2014a). These two semi-empirical geothermometers were calibrated with the idea that iron in chlorite must be expressed as $\text{Fe}_{\text{tot}} = \text{Fe}^{2+} + \text{Fe}^{3+}$. As demonstrated by Figure 11 there is no general relation between Fe^{3+} and T except for given redox conditions (in this case, $X_{\text{Fe}^{3+}}$ increases with decreasing T). The results of this study confirm the existence of a highly oxidized trend that was before only predicted by modeling and prove that $X_{\text{Fe}^{3+}}$ in chlorite can reach 45%. This result demonstrates that chlorite may be used to investigate the redox conditions in low-grade metamorphic rocks and hydrothermal environments. Fe^{3+} end-members must be defined and should be used in the framework of thermodynamic modeling. This is an important domain for further research in chlorite geothermometry and the results reported in this study provide first importance data to adjust such models.

(3) The quantitative micro-mapping technique used in this study is fundamental to highlight variations of chemistry in 2D at the thin section scale. This method allows to measure the chemical heterogeneity of minerals and to calculate maps of formation temperature, which are critical to see the relations between T and the geometry of the crystals. Here we demonstrate that this method may be coupled with single-spot μ -XANES analyses to generate maps of structural formulas (Fig. 10) with variable $X_{\text{Fe}^{3+}}$. This offers new opportunities to apply the same strategy using other high-precision instruments such as LA-ICP-MS or SIMS.

(4) This paper demonstrates that the temperature of the fluid within a vein is an important parameter that controls the composition of the growing minerals. The zoned chlorite crystals record changes that are caused by hot fluids pulses intercalated with cooling periods. The process of fault-valve behavior is an important process to explain the crystallization of this chlorite in the PPV thrust veins. The detailed study of phyllosilicates can help to better understand fluid flows in a fault and to investigate the relations of such flows with the seismic activity of the thrust. The future results obtained using the strategy detailed in this study may have large implications in geosciences.

ACKNOWLEDGMENTS

This work was supported by the French RENATECH network and its FEMTO-ST technological facility. Micro-XANES measurements were supported by In-House research program of the BM23 beamline of the ESRF. We particularly thank O. Mathon for his crucial help during data acquisition. We address our thanks to E. Courgeon, guardian of Barroude refuge for his pictures and his hospitality

and to O. Fabbri for English proofreading. Authors warmly thank A.M. Boullier for discussions on the genetic model. We also thank the editor D. Dyar and detailed reviews by O. Tarantola and A. McCaig, which allowed improving this manuscript, especially the discussion section.

REFERENCES CITED

- Banks, D.A., and Yardley, B.W.D. (1992) Crush-leach analysis of fluid inclusions in small natural and synthetic samples. *Geochimica et Cosmochimica Acta*, 56, 245–248.
- Banks, D., Davies, G., Yardley, B.W., McCaig, A., and Grant, N. (1991) The chemistry of brines from an Alpine thrust system in the Central Pyrenees: An application of fluid inclusion analysis to the study of fluid behaviour in orogenesis. *Geochimica et Cosmochimica Acta*, 55, 1021–1030.
- Beaufort, D., Patrier, P., Meunier, A., and Ottaviani, M.M. (1992) Chemical variations in assemblages including epidote and/or chlorite in the fossil hydrothermal system of Saint Martin (Lesser Antilles). *Journal of Volcanology and Geothermal Research*, 51, 95–114.
- Beaufort, D., Patrier, P., Laverret, E., Bruneton, P., and Mondy, J. (2005) Clay alteration associated with proterozoic unconformity-type uranium deposits in the East Alligator Rivers Uranium Field, Northern Territory, Australia. *Economic Geology*, 100, 515–536.
- Blanco-Quintero, I.F., García-Casco, A., and Gerya, T.V. (2011) Tectonic blocks in serpentinite mélange (eastern Cuba) reveal large-scale convective flow of the subduction channel. *Geology*, 39, 79–82.
- Bons, P.D., Elburg, M.A., and Gomez-Rivas, E. (2012) A review of the formation of tectonic veins and their microstructures. *Journal of Structural Geology*, 43, 33–62.
- Borg, S., Liu, W., Pearce, M., Cleverly, J., and MacRae, C. (2014) Complex mineral zoning patterns caused by ultra-local equilibrium at reaction interfaces. *Geology*, <http://dx.doi.org/10.1130/G35287.1>.
- Bos, B., and Spiers, C.J. (2001) Experimental investigation into the microstructural and mechanical evolution of phyllosilicate-bearing fault rock under conditions favouring pressure solution. *Journal of Structural Geology*, 23, 1187–1202.
- Boullier, A.-M., and Robert, F. (1992) Palaeoseismic events recorded in Archaean gold-quartz vein networks, Val d'Or, Abitibi, Quebec, Canada. *Journal of Structural Geology*, 14, 161–179.
- Bourdelle, F., Parra, T., Beyssac, O., Chopin, C., and Vidal, O. (2013) Clay minerals as geo-thermometer: A comparative study based on high spatial resolution analysis of illite and chlorite in Gulf Coast sandstones (Texas, U.S.A.). *American Mineralogist*, 98, 914–926.
- Brodsky, E.E., Rowe, C.D., Meneghini, F., and Moore, J.C. (2009) A geological fingerprint of low-viscosity fault fluids mobilized during an earthquake. *Journal of Geophysical Research: Solid Earth*, 114, B01303.
- Brun, J.P., and Cobbold, P.R. (1980) Strain heating and thermal softening in continental shear zones: a review. *Journal of Structural Geology*, 2, 149–158.
- Buatier, M.D., Lacroix, B., Labaume, P., Moutartier, V., Charpentier, D., Sizun, J.P., and Travé, A. (2012) Microtextural investigation (SEM and TEM study) of phyllosilicates in a major thrust fault zone (Monte Perdido, southern Pyrenees): Impact on fault reactivation. *Swiss Journal of Geosciences*, 105, 313–324.
- Cantarero, I., Lanari, P., Vidal, O., Aliás, G., Travé, A., and Baqués, V. (2014) Long-term fluid circulation in extensional faults in the central Catalan Coastal Ranges: P-T constraints from neofomed chlorite and K-white mica. *International Journal of Earth Sciences*, 103, 165–188.
- Carslaw, H.S., Jaeger, J.C., and others. (1959) *Conduction of Heat in Solids*, Vol. 2. Clarendon Press, Oxford.
- Cathelineau, M. (1988) Cation site occupancy in chlorites and illites as a function of temperature. *Clay Minerals*, 23, 471–485.
- Cathelineau, M., and Nieva, D. (1985) A chlorite solid solution geothermometer the Los Azufres (Mexico) geothermal system. *Contributions to Mineralogy and Petrology*, 91, 235–244.
- Chester, F.M., Evans, J.P., and Biegel, R.L. (1993) Internal structure and weakening mechanisms of the San Andreas Fault. *Journal of Geophysical Research: Solid Earth*, 98, 771–786.
- Dare, S.A.S., Barnes, S.-J., Prichard, H.M., and Fisher, P.C. (2011) Chalcophile and platinum-group element (PGE) concentrations in the sulfide minerals from the McCreeby East deposit, Sudbury, Canada, and the origin of PGE in pyrite. *Mineralium Deposita*, 46, 381–407.
- De Andrade, V., Vidal, O., Lewin, E., O'Brien, P., and Agard, P. (2006) Quantification of electron microprobe compositional maps of rock thin sections: an optimized method and examples RID C-2856-2009. *Journal of Metamorphic Geology*, 24, 655–668.
- De Caritat, P., Hutcheon, I., and Walshe, J.L. (1993) Chlorite geothermometry; a review. *Clays and Clay Minerals*, 41, 219–239.
- De Grave, E., Vandenbruwaene, J., and Bockstael, M.V. (1987) ⁵⁷Fe Mössbauer spectroscopic analysis of chlorite. *Physics and Chemistry of Minerals*, 15, 173–180.
- Delvigne, J.E. (1998) *Atlas of Micromorphology of Mineral Alteration and Weathering*, 520 p. Mineralogical Association of Canada, Québec.
- Dowty, E. (1976) Crystal structure and crystal growth; II, Sector zoning in minerals. *American Mineralogist*, 61, 460–469.
- Dziggel, A., Wulff, K., Kolb, J., Meyer, F.M., and Lahaye, Y. (2009) Significance of oscillatory and bell-shaped growth zoning in hydrothermal garnet: Evidence from the Navachab gold deposit, Namibia. *Chemical Geology*, 262, 262–276.
- Friel, J.J., and Lyman, C.E. (2006) Tutorial review: X-ray mapping in electron-beam instruments. *Microscopy and Microanalysis*, 12, 2–25.
- Gaidies, F., Capitani, C. de, Abart, R., and Schuster, R. (2008) Prograde garnet growth along complex P–T paths: results from numerical experiments on polyphase garnet from the Wölz Complex (Austroalpine basement). *Contributions to Mineralogy and Petrology*, 155, 673–688.
- García-Casco, A., Torres-Roldán, R.L., Millán, G., Monié, P., and Schneider, J. (2002) Oscillatory zoning in eclogitic garnet and amphibole, Northern Serpentinite Melange, Cuba: a record of tectonic instability during subduction? *Journal of Metamorphic Geology*, 20, 581–598.
- Gaspar, M., Knaack, C., Meinert, L.D., and Moretti, R. (2008) REE in skarn systems: A LA-ICP-MS study of garnets from the Crown Jewel gold deposit. *Geochimica et Cosmochimica Acta*, 72, 185–205.
- Grant, N.T. (1989) Deformation and fluid processes in thrust sheets from the central Pyrenees. Ph.D. thesis, University of Leeds, U.K.
- (1990) Episodic discrete and distributed deformation: consequences and controls in a thrust culmination from the central Pyrenees. *Journal of Structural Geology*, 12, 835–850.
- (1992) Post-emplacement extension within a thrust sheet from the central Pyrenees. *Journal of the Geological Society*, 149, 775–792.
- Grant, N.T., Banks, D.A., McCaig, A.M., and Yardley, B.W.D. (1990) Chemistry, source, and behavior of fluids involved in Alpine thrusting of the Central Pyrenees. *Journal of Geophysical Research*, 95, 9123–9131.
- Grosch, E.G., Vidal, O., Abu-Alam, T., and McLoughlin, N. (2012) P-T constraints on the metamorphic evolution of the Paleoproterozoic Kromberg Type-Section, Barberton Greenstone Belt, South Africa. *Journal of Petrology*, 53, 513–545.
- Haines, S.H., and van der Pluijm, B.A. (2012) Patterns of mineral transformations in clay gouge, with examples from low-angle normal fault rocks in the western USA. *Journal of Structural Geology*, 43, 2–32.
- Hayes, J.B. (1970) Polytypism of chlorite in sedimentary rocks. *Clays and Clay Minerals*, 18, 285–306.
- Hillier, S., and Velde, B. (1991) Octahedral occupancy and chemical composition of diagenetic (low-temperature) chlorites. *Clay Minerals*, 26, 149–168.
- Holdsworth, R.E. (2004) Weak faults—Rotten cores. *Science*, 303, 181–182.
- Holten, T., Jamtveit, B., Meakin, P., Cortini, M., Blundy, J., and Austrheim, H. (1997) Statistical characteristics and origin of oscillatory zoning in crystals. *American Mineralogist*, 82, 596–606.
- Holten, T., Jamtveit, B., and Meakin, P. (2000) Noise and oscillatory zoning of minerals. *Geochimica et Cosmochimica Acta*, 64, 1893–1904.
- Inoue, A., Meunier, A., Patrier-Mas, P., Rigault, C., Beaufort, D., and Vieillard, P. (2009) Application of chemical geothermometry to low-temperature trioctahedral chlorites. *Clays and Clay Minerals*, 57, 371–382.
- Jamtveit, B. (1991) Oscillatory zonation patterns in hydrothermal grossular-andradite garnet; nonlinear dynamics in regions of immiscibility. *American Mineralogist*, 76, 1319–1327.
- Jamtveit, B., and Andersen, T.B. (1992) Morphological instabilities during rapid growth of metamorphic garnets. *Physics and Chemistry of Minerals*, 19, 176–184.
- Jamtveit, B., Wogelius, R.A., and Fraser, D.G. (1993) Zonation patterns of skarn garnets: Records of hydrothermal system evolution. *Geology*, 21, 113–116.
- Jolivet, M., Labaume, P., Monié, P., Brunel, M., Arnaud, N., and Campani, M. (2007) Thermochronology constraints for the propagation sequence of the south Pyrenean basement thrust system (France-Spain). *Tectonics*, 26, TC5007.
- Jourdan, A.-L., Vennemann, T.W., Mullis, J., Ramseyer, K., and Spiers, C.J. (2009) Evidence of growth and sector zoning in hydrothermal quartz from Alpine veins. *European Journal of Mineralogy*, 21, 219–231.
- Kohn, M.J. (2003) Geochemical zoning in metamorphic minerals. *The Crust*, 3, 229–261.
- Kohn, M.J., and Spear, F. (2000) Retrograde net transfer reaction insurance for pressure-temperature estimates. *Geology*, 28, 1127–1130.
- Kwak, T.A.P. (1981) Sector-zoned annite 85 phlogopite 15 micas from the Mt. Lindsay Sn-W-F-(Be) deposit, Tasmania, Australia. *Canadian Mineralogist*, 19, 643–650.
- Lacroix, B., and Vennemann, T. (2015) Empirical calibration of the oxygen isotope fractionation between quartz and Fe–Mg-chlorite. *Geochimica et Cosmochimica Acta*, 149, 21–31.
- Lacroix, B., Buatier, M., Labaume, P., Travé, A., Dubois, M., Charpentier, D., Ventalon, S., and Convert-Gaubier, D. (2011) Microtectonic and geochemical characterization of thrusting in a foreland basin: Example of the South-Pyrenean orogenic wedge (Spain). *Journal of Structural Geology*, 33, 1359–1377.
- Lacroix, B., Charpentier, D., Buatier, M., Vennemann, T., Labaume, P., Adatte, T., Trave, A., and Dubois, M. (2012) Formation of chlorite during thrust fault reactivation. Record of fluid origin and P-T conditions in the Monte Perdido thrust fault (southern Pyrenees). *Contributions to Mineralogy and Petrology*, 163, 1083–1102.
- Lacroix, B., Travé, A., Buatier, M., Labaume, P., Vennemann, T., and Dubois, M. (2014) Syntectonic fluid-flow along thrust faults: Example of the South-Pyrenean fold-and-thrust belt. *Marine and Petroleum Geology*, 49, 84–98.
- Lanari, P., Guillot, S., Schwartz, S., Vidal, O., Tricart, P., Riel, N., and Beyssac, O. (2012) Diachronous evolution of the alpine continental subduction wedge: Evidence from P–T estimates in the Briançonnais Zone houillère (France, Western Alps). *Journal of Geodynamics*, 56–57, 39–54.

- Lanari, P., Riel, N., Guillot, S., Vidal, O., Schwartz, S., Pêcher, A., and Hattori, K.H. (2013) Deciphering high-pressure metamorphism in collisional context using microprobe mapping methods: Application to the Stak eclogitic massif (northwest Himalaya). *Geology*, 41, 111–114.
- Lanari, P., Wagner, T., and Vidal, O. (2014a) A thermodynamic model for di-trioctahedral chlorite from experimental and natural data in the system $MgO-FeO-Al_2O_3-SiO_2-H_2O$: applications to P-T sections and geothermometry. *Contributions to Mineralogy and Petrology*, 167, 1–19.
- Lanari, P., Vidal, O., De Andrade, V., Dubacq, B., Lewin, E., Grosch, E.G., and Schwartz, S. (2014b) XMapTools: A MATLAB®-based program for electron microprobe X-ray image processing and geothermobarometry. *Computers & Geosciences*, 62, 227–240.
- Leclère, H., Buatier, M., Charpentier, D., Sizun, J.-P., Labaume, P., and Cavailles, T. (2012) Formation of phyllosilicates in a fault zone affecting deeply buried arkosic sandstones: their influence on petrophysical properties (Annot sandstones, French external Alps). *Swiss Journal of Geosciences*, 105, 299–312.
- Leclère, H., Lacroix, B., and Fabbri, O. (2014) Fault mechanics at the base of the continental seismogenic zone: Insights from geochemical and mechanical analyses of a crustal-scale transpressional fault from the Argentera crystalline massif, French–Italian Alps. *Journal of Structural Geology*, 66, 115–128.
- Manga, M., and Wang, C.Y. (2007) Earthquake hydrology. *Treatise on Geophysics*, 4, 29.
- Manzotti, P., and Ballèvre, M. (2013) Multistage garnet in high-pressure metasediments: Alpine overgrowths on Variscan detrital grains. *Geology*, 41, 1151–1154.
- Martin, C., Debaille, V., Lanari, P., Goderis, S., Vandendael, I., Vanhaecke, F., Vidal, O., and Claey, P. (2013) REE and Hf distribution among mineral phases in the CV–CK clan: A way to explain present-day Hf isotopic variations in chondrites. *Geochimica et Cosmochimica Acta*, 120, 496–513.
- McCaig, A.M., Wayne, D.M., Marshall, J.D., Banks, D., and Henderson, I. (1995) Isotopic and fluid inclusion studies of fluid movement along the Gavarnie Thrust, central Pyrenees; reaction fronts in carbonate mylonites. *American Journal of Science*, 295, 309–343.
- McCaig, A.M., Wayne, D., and Rosenbaum, J. (2000) Fluid expulsion and dilatancy pumping during thrusting in the Pyrenees: Pb and Sr isotope evidence. *Geological Society of America Bulletin*, 112, 1199–1208.
- Merlet, C., and Bodinier, J.-L. (1990) Electron microprobe determination of minor and trace transition elements in silicate minerals: A method and its application to mineral zoning in the peridotite nodule PHN 1611. *Chemical Geology*, 83, 55–69.
- Meth, C.E., and Carlson, W.D. (2005) Diffusion-controlled synkinematic growth of garnet from a heterogeneous precursor at Passo Del Sole, Switzerland. *Canadian Mineralogist*, 43, 157–182.
- Mogi, K., Mochizuki, H., and Kurokawa, Y. (1989) Temperature changes in an artesian spring at Usami in the Izu Peninsula (Japan) and their relation to earthquakes. *Tectonophysics*, 159, 95–108.
- Muñoz, J.A. (1992) Evolution of a continental collision belt: ECORS-Pyrenees crustal balanced cross-section. In K.R. McClay, Ed., *Thrust Tectonics*, pp. 235–246. Springer Netherlands, Dordrecht.
- Muñoz, M., De Andrade, V., Vidal, O., Lewin, E., Pascarelli, S., and Susini, J. (2006) Redox and speciation micromapping using dispersive X-ray absorption spectroscopy: Application to iron chlorite mineral of a metamorphic rock thin section. *Geochemistry Geophysics Geosystems*, 7, Q11020.
- Muñoz, M., Pascarelli, S., Aquilanti, G., Narygina, O., Kurnosov, A., and Dubrovinsky, L. (2008) Hyperspectral μ -XANES mapping in the diamond-anvil cell: analytical procedure applied to the decomposition of (Mg,Fe)-ringwoodite at the upper/lower mantle boundary. *High Pressure Research*, 28, 665–673.
- Muñoz, M., Vidal, O., Marcellou, C., Pascarelli, S., Mathon, O., and Farges, F. (2013) Iron oxidation state in phyllosilicate single crystals using Fe-K pre-edge and XANES spectroscopy: Effects of the linear polarization of the synchrotron X-ray beam. *American Mineralogist*, 98, 1187–1197.
- Nicotra, E., and Viccaro, M. (2012) Unusual magma storage conditions at Mt. Etna (Southern Italy) as evidenced by plagioclase megacryst-bearing lavas: implications for the plumbing system geometry and summit caldera collapse. *Bulletin of Volcanology*, 74, 795–815.
- Pearce, M.A., and Wheeler, J. (2010) Modelling grain-recycling zoning during metamorphism. *Journal of Metamorphic Geology*, 28, 423–437.
- Pfalter, P., Urbach, J.-P., Klemm, M., and Horn, S. (1999) Elimination of self-absorption in fluorescence hard-X-ray absorption spectra. *Physical Review B*, 60, 9335–9339.
- Putirka, K.D., and Tepley, F.J. (2008) Minerals, Inclusions and Volcanic Processes. *Reviews in Mineralogy and Geochemistry*, Mineralogical Society of America, Chantilly, Virginia.
- Rahl, J.M., Haines, S.H., and van der Pluijm, B.A. (2011) Links between orogenic wedge deformation and erosional exhumation: Evidence from illite age analysis of fault rock and detrital thermochronology of syn-tectonic conglomerates in the Spanish Pyrenees. *Earth and Planetary Science Letters*, 307, 180–190.
- Ramsay, J.G. (1980) The crack-seal mechanism of rock deformation. *Nature*, 284, 135–139.
- Robyr, M., Carlson, W.D., Passchier, C., and Vonlanthen, P. (2009) Microstructural, chemical and textural records during growth of snowball garnet. *Journal of Metamorphic Geology*, 27, 423–437.
- Robyr, M., Darbellay, B., and Baumgartner, L.P. (2014) Matrix-dependent garnet growth in polymetamorphic rocks of the Sesia zone, Italian Alps. *Journal of Metamorphic Geology*, 32, 3–24.
- Roure, F., Choukroune, P., Berastegui, X., Munoz, J.A., Villien, A., Matheron, P., Bareyt, M., Seguret, M., Camara, P., and Deramond, J. (1989) Ecorep deep seismic data and balanced cross sections: Geometric constraints on the evolution of the Pyrenees. *Tectonics*, 8, 41–50.
- Schumacher, R., Roetzel, K., and Maresch, W.V. (1999) Subtle oscillatory zoning in garnet from regional metamorphic phyllites and mica schists, western Erzgebirge, Germany. *Canadian Mineralogist*, 37, 381–403.
- Shata, S., and Hesse, R. (1998) A refined XRD method for the determination of chlorite composition and application to the McGerrigle Mountains anchizone in the Quebec Appalachians. *Canadian Mineralogist*, 36, 1525–1546.
- Shcherbakov, V.D., Plechov, P.Y., Izbekov, P.E., and Shipman, J.S. (2011) Plagioclase zoning as an indicator of magma processes at Bezymianny Volcano, Kamchatka. *Contributions to Mineralogy and Petrology*, 162, 83–99.
- Shore, M., and Fowler, A.D. (1996) Oscillatory zoning in minerals; a common phenomenon. *Canadian Mineralogist*, 34, 1111–1126.
- Sibson, R.H. (1990) Conditions for fault-valve behaviour. *Geological Society, London, Special Publications*, 54, 15–28.
- Souche, A., Medvedev, S., Andersen, T.B., and Dabrowski, M. (2013) Shear heating in extensional detachments: Implications for the thermal history of the Devonian basins of W Norway. *Tectonophysics*, 608, 1073–1085.
- Tarantola, A., Mullis, J., Guillaume, D., Dubessy, J., de Capitani, C., and Abdelmoula, M. (2009) Oxidation of CH_4 to CO_2 and H_2O by chloritization of detrital biotite at 270 \pm 5 $^{\circ}C$ in the external part of the Central Alps, Switzerland. *Lithos*, 112, 497–510.
- Teixell, A. (1996) The Anso transect of the southern Pyrenees: basement and cover thrust geometries. *Journal of the Geological Society*, 153, 301–310.
- (1998) Crustal structure and orogenic material budget in the west central Pyrenees. *Tectonics*, 17, 395–406.
- (2000) Geotectónica de los Pirineos. *Investigación y Ciencia*, 288, 54–65.
- Toutain, J.P., Munoz, M., Poitras, F., and Lienard, A.C. (1997) Springwater chloride ion anomaly prior to a $M_L=5.2$ Pyrenean earthquake. *Earth and Planetary Science Letters*, 149, 113–119.
- Toutain, J.-P., Munoz, M., Pinaud, J.-L., Levet, S., Sylvander, M., Rigo, A., and Escalier, J. (2006) Modelling the mixing function to constrain coseismic hydrochemical effects: An example from the French Pyrénées. *Pure and Applied Geophysics*, 163, 723–744.
- Trincal, V., Charpentier, D., Buatier, M.D., Grobety, B., Lacroix, B., Labaume, P., and Sizun, J.-P. (2014) Quantification of mass transfers and mineralogical transformations in a thrust fault (Monte Perdido thrust unit, southern Pyrenees, Spain). *Marine and Petroleum Geology*, 55, 160–175.
- Vidal, O., Parra, T., and Trotet, F. (2001) A thermodynamic model for Fe-Mg aluminous chlorite using data from phase equilibrium experiments and natural pelitic assemblages in the 100 degrees to 600 $^{\circ}C$, 1 to 25 kb range. *American Journal of Science*, 301, 557–592.
- Vidal, O., Parra, T., and Vieillard, P. (2005) Thermodynamic properties of the Tschermak solid solution in Fe-chlorite: Application to natural examples and possible role of oxidation. *American Mineralogist*, 90, 347–358.
- Vidal, O., De Andrade, V., Lewin, E., Muñoz, M., Parra, T., and Pascarelli, S. (2006) P-T-deformation- Fe^{3+}/Fe^{2+} mapping at the thin section scale and comparison with XANES mapping: application to a garnet-bearing metapelite from the Sambagawa metamorphic belt (Japan). *Journal of Metamorphic Geology*, 24, 669–683.
- Walker, J.R. (1993) Chlorite polytype geothermometry. *Clays and Clay Minerals*, 41, 260–267.
- Wang, C., and Manga, M. (2010) *Earthquakes and Water*, vol. 114. Springer, Berlin.
- Wang, Y., and Merino, E. (1992) Dynamic model of oscillatory zoning of trace elements in calcite: Double layer, inhibition, and self-organization. *Geochimica et Cosmochimica Acta*, 56, 587–596.
- Wilke, M., Farges, F., Petit, P.-E., Brown, G.E., and Martin, F. (2001) Oxidation state and coordination of Fe in minerals: An Fe K-XANES spectroscopic study. *American Mineralogist*, 86, 714–730.
- Wintsch, R.P., Christoffersen, R., and Kronenberg, A.K. (1995) Fluid-rock reaction weakening of fault zones. *Journal of Geophysical Research*, 100, 13,021–13,032.
- Yardley, B.W.D., Rochelle, C.A., Bamicoat, A.C., and Lloyd, G.E. (1991) Oscillatory zoning in metamorphic minerals: an indicator of infiltration metasomatism. *Mineralogical Magazine*, 55, 357–365.
- Zane, A., Sassi, R., and Guidotti, C.V. (1998) New data on metamorphic chlorite as a petrogenetic indicator mineral, with special regard to greenschist-facies rocks. *Canadian Mineralogist*, 36, 713–726.
- Zhai, D.-G., Liu, J.-J., Zhang, H.-Y., Wang, J.-P., Su, L., Yang, X.-A., and Wu, S.-H. (2014) Origin of oscillatory zoned garnets from the Xicertala Fe–Zn skarn deposit, northern China: In situ LA-ICP-MS evidence. *Lithos*, 190–191, 279–291.